Monthly Notices of the ROYAL ASTRONOMICAL SOCIETY

MNRAS **545,** 1–14 (2026) https://doi.org/10.1093/mnras/staf2009
Advance Access publication 2025 November 14

Effect of spin in binary neutron star mergers

Beyhan Karakaş,★† Rahime Matur [1]★ and Maximilian Ruffert [2]

[1]*Mathematical Sciences and STAG Research Centre, University of Southampton, Southampton SO17 1BJ, UK*
[2]*School of Mathematics and Maxwell Institute, University of Edinburgh, Edinburgh EH9 3FD, UK*

Accepted 2025 November 11. Received 2025 November 11; in original form 2024 June 21

ABSTRACT

We investigate the effect of spin on equal- and unequal-mass binary neutron star mergers using finite-temperature, composition-dependent Steiner–Fischer–Hempel equation of state with parameter set 'o', via 3 + 1 general relativistic hydrodynamics simulations, which take into account neutrino emission and absorption. Equal-mass, irrotational cases that have a mass of $M_{1,2} = 1.27$ M$_\odot$ result in a long-lived neutron star, while 1.52 and 2.05 M$_\odot$ cases lead to a prompt collapse to a black hole. For all cases, we analyse the effect of initial spin on dynamics, on the structure of the final remnant, its spin evolution, the amount and composition of the ejected matter, gravitational waves, neutrino energies and luminosities, and disc masses. We show that in equal-mass binary neutron star mergers, the ejected mass could reach ∼0.06 M$_\odot$ for highly aligned spins ($\chi = 0.67$). The black hole that results from such a highly spinning, high-mass binary neutron star merger reaches a dimensionless spin of 0.92; this is the highest spin reached in binary neutron star mergers, to date.

Key words: gravitational waves – hydrodynamics – neutrinos – stars: neutron – stars: rotation – neutron star mergers.

1 INTRODUCTION

The detection of the gravitational wave (GW) event GW170817 (B. P. Abbott et al. 2017a) by the Advanced Laser Interferometer Gravitational-wave Observatory (LIGO) (The LIGO Scientific Collaboration 2015) and Advanced Virgo (F. Acernese et al. 2015) detectors corresponded to the inspiral phase of a binary neutron star (BNS) merger. Its electromagnetic (EM) counterpart, EM170817 (M. M. Kasliwal et al. 2017), which included the short Gamma-Ray Burst (sGRB) GRB170817A, provided the first direct confirmation of the long-anticipated association between BNS mergers and sGRBs (D. Eichler et al. 1989; T. Piran 1992; M. Ruffert, H. T. Janka & G. Schäfer 1995; M. Ruffert et al. 1997; M. Ruffert & H. T. Janka 2001; B. P. Abbott et al. 2017b, c; A. Goldstein et al. 2017; T. Dietrich et al. 2020). Beyond this milestone, GW170817 offered pivotal insights into neutron star (NS) physics. By assuming low spin priors and using observed NS masses, it constrained NS spins (B. P. Abbott et al. 2019a) and the equation of state (EoS), ruling out both very soft and very stiff EoSs. Building on these EoS constraints, the maximum Tolman-Oppenheimer-Volkoff (TOV) mass is estimated to lie within the range (1.97 M$_\odot$ < $M_{\rm max}$ < 2.17 M$_\odot$) (B. Margalit & B. D. Metzger 2017; D. Radice et al. 2018a; The LIGO Scientific Collaboration & The Virgo Collaboration 2018; B. P. Abbott et al. 2019a). Additionally, GW170817 strengthened evidence for BNS mergers as sites of r-process nucleosynthesis and kilonovae (G. Hallinan et al. 2017; D. Kasen et al. 2017; E. Pian et al. 2017; S. J. Smartt et al. 2017; E. Troja et al. 2017), provided a strong test of general relativity in the strong gravity regime (B. P. Abbott et al. 2019b), and placed constraints on alternative theories of gravity (T. Baker et al. 2017; J. Sakstein & B. Jain 2017).

The current detectors are sensitive mainly to the inspiral phase of BNS mergers, enabling the measurement of three key parameters: chirp mass $\mathcal{M}$ (P. Kafka 1988; C. Cutler et al. 1993; L. S. Finn & D. F. Chernoff 1993; C. Cutler & E. Flanagan 1994), effective spin $\chi = (M_1\chi_1\cos\theta_1 + M_2\chi_2\cos\theta_2)/(M_1 + M_2)$, where $\chi_{1,2}$ are the dimensionless spin magnitudes, $\theta_{1,2}$ are the angles between the spin vectors and the orbital angular momentum, and $M_{1,2}$ are the masses of each star, and tidal deformability parameter of the binary Λ (E. E. Flanagan & T. Hinderer 2008; T. Hinderer 2008; T. Hinderer et al. 2010; J. S. Read et al. 2013; B. P. Abbott et al. 2017c). For GW170817, assuming high spin priors for the components aligned with the orbital angular momentum ($|\chi| \leq 0.89$), these parameters were measured as $\mathcal{M} = 1.188^{+0.004}_{-0.002}$ M$_\odot$, $\chi \in (0.0, 0.09)$, and $\Lambda <$ 800 (at 90 per cent credible interval) (B. P. Abbott et al. 2017a). Among these, tidal deformability is particularly important for extracting EoS information from GWs. However, a recent study by F. Gittins et al. (2025) quantitatively demonstrated that this calculation can be affected by artificial heating of the stars, which introduces significant systematics. Unlike GW170817, another BNS merger, GW190425 (B. P. Abbott et al. 2020), was observed solely via GWs. By assuming high spin priors, the effective spin for GW190425 was measured as $\chi = 0.058^{+0.11}_{-0.05}$.

To accurately interpret GW observations in BNS mergers, it is essential to perform numerical simulations with well-controlled and systematically varied spin configurations, starting from consistent initial data (ID). Theoretical efforts to create spinning BNS ID began with P. Marronetti & S. L. Shapiro (2003), and were further explored in studies by W. Kastaun et al. (2013), L. J. Papenfort et al. (2021), A. Rashti & A. Noe (2025), N. Tacik et al. (2015), W. Tichy (2006,

★ E-mail: beyhannkarakas@gmail.com (BK); r.matur@soton.ac.uk (RM)
† Fellow of the Royal Astronomical Society.

2009a, b, 2011, 2012), W. Tichy et al. (2019), and P. Tsatsin & P. Marronetti (2013). While these studies focused on constructing spinning ID, state-of-the-art BNS merger simulations now address increasingly complex aspects of these systems, including turbulence modelling, neutrino transport, and computational efficiency. Key advancements include subgrid-scale turbulence modelling, which serves as an alternative to ultra-high-resolution (ultra-HR) general relativistic magnetohydrodynamics simulations (D. Radice 2017, 2020; D. Radice et al. 2018c), see also D. Radice & I. Hawke (2024) for a recent review on the impact of turbulence in BNS mergers. Additional advancements include improved vacuum treatment (A. Poudel et al. 2020), using discontinuous Galerkin method (W. Tichy et al. 2023; N. Deppe et al. 2024), and the combination of fixed mesh refinement with smoothed particle hydrodynamics (S. Rosswog, F. Torsello & P. Diener 2023; S. Rosswog et al. 2024). Furthermore, improved neutrino transport models have been developed (F. Foucart et al. 2021, 2024; D. Radice et al. 2022), with their significance highlighted in a recent review (F. Foucart 2023). Finally, graphics processing unit (GPU)-based simulations have been reported to demonstrate an order-of-magnitude speed-up over central processing unit (CPU)-based simulations of these systems (J. Fields et al. 2025).

Building on advancements in BNS merger simulations, several studies have investigated the impact of spin. Among these, W. Kastaun et al. (2013) was the first to investigate how the initial spin affects the maximum spin of the final black hole (BH) in equal-mass models that promptly collapse to a BH. They reported an upper limit of $\chi = 0.88 \pm 0.018$ and identified, for the first time, the orbital hang-up effect, a repulsive spin–orbit interaction observed in systems with spins aligned with the orbital angular momentum. This phenomenon had previously been reported in binary BH (BBH) (M. Campanelli, C. O. Lousto & Y. Zlochower 2006), and BH–NS mergers (Z. B. Etienne et al. 2009). Subsequent investigations by S. Bernuzzi et al. (2014) and T. Dietrich et al. (2017b) confirmed this finding. Notably, S. Bernuzzi et al. (2014) extended these investigations to include anti-aligned spin BNS merger simulations. Their results demonstrated that anti-aligned spin models merge faster, a phenomenon called 'speed-up', as compared to the irrotational model. This behaviour was consistent with earlier findings in BBH mergers (M. Campanelli et al. 2006). They also reported a shift in the peak frequency of the fundamental mode f_2, corresponding to the $(l, m) = (2, 2)$ mode, towards lower frequencies for aligned spins of $\chi = 0.05$.

While earlier studies used simple gamma-law EoSs, W. Kastaun & F. Galeazzi (2015) were the first to employ microphysical EoSs to investigate spinning BNS mergers. Their work examined equal-mass spinning (aligned) and irrotational models, as well as unequal-mass irrotational models that primarily form long-lived NSs. They reported that the rotation profile of the remnant differed from predictions based on a single, differentially rotating NS, with the remnant core rotating more slowly than the envelope. T. Dietrich et al. (2015b) presented the first precessing BNS merger simulation, along with the most asymmetric mass ratio, $q = 2.06$, where $q = M_1/M_2 \geq 1$ is defined as the ratio of the mass of the more massive star (M_1) to that of the less massive star (M_2). They observed modulation in the $(l, m) = (2, 1)$ mode of GWs due to precession and reported a shift in f_2, similar to the findings of S. Bernuzzi et al. (2014). Similarly, N. Tacik et al. (2015) investigated spin effects on orbital dynamics, including aligned, anti-aligned, and misaligned spins. They found that although spin direction changes during the late inspiral, its magnitude remains conserved.

T. Dietrich et al. (2017b) extended these investigations to equal- and unequal-mass binaries, $q \leq 1.5$ with aligned, anti-aligned, or just one component spins. Their results showed that spin alignment (anti-alignment) with orbital angular momentum increases (decreases) mass ejection compared to irrotational models. They also reported the f_2 mode frequency shift previously identified in S. Bernuzzi et al. (2014) and T. Dietrich et al. (2015b). In equal-mass precessing BNS mergers, T. Dietrich et al. (2018) found that spin precession does not influence post-merger GW frequencies and mass ejection.

W. E. East et al. (2019) explored equal-mass spinning BNS mergers with spins aligned and anti-aligned with the orbital angular momentum, considering a maximum spin of $\chi = 0.33$. They reported that the dependence of the one-arm, $m = 1$, instability on spin is weak (V. Paschalidis et al. 2015; W. E. East et al. 2016; D. Radice, S. Bernuzzi & C. D. Ott 2016a). The frequency of the $m = 1$ mode, f_1, which corresponds to $(l, m) = (2, 1)$ mode was observed to shift to lower values for aligned spins. Anti-aligned spin models produce more massive ejecta, while aligned spins reduce ejecta mass up to $\chi = 0.17$, after which it increases, equalling the ejecta mass of the irrotational model at $\chi = 0.3$.

S. V. Chaurasia et al. (2020) recently investigated the influence of spin orientation on GW and mass ejection, showing that for equal-mass models with the maximum effective spin magnitude of 0.096 in aligned and anti-aligned spins, the lifetime of the remnant NS depends primarily on the effective spin magnitude rather than the spin orientation. They reported anisotropic ejecta distribution in precessing mergers. R. Dudi et al. (2022) studied high spin models, $-0.28 \leq \chi \leq 0.58$, finding that aligned spins produce more ejecta and disc mass than anti-aligned spins, with disc wind ejecta showing spin dependence. L. J. Papenfort et al. (2022) analysed single-spin aligned models ($\chi_1 = 0.30,\ 0.40,\ 0.60$) with mass ratios $1 \leq q \leq 1.67$, using the TNTYST (a variational nuclear EoS) and BHB$\Lambda\Phi$ (a hadronic EoS that includesΛ hyperons at high densities) EOSs.They found that higher mass ratio systems yield longer lived remnants than the equal-mass binaries, and that disc and ejecta masses increase with both mass ratio and spin. The largest amount of dynamical ejecta occurred for $\chi_1 = 0.60$ with $q = 1$. Similarly, focusing on a single-spin aligned model, $\chi_1 = 0.5$, S. Rosswog et al. (2024) investigated equal-mass BNS mergers and found that spinning models result in less violent mergers and significantly brighter kilonovae as compared to irrotational models. They also explored the dependence of f_2 on the EoS, showing that the softest EoS (SLy) exhibited the highest frequency shift, while the stiffest EoS (MS1b) showed no detectable shift. Moreover, F. Schianchi et al. (2024) investigated the impact of spin on BH formation using piecewise-polytropic SLy and H4 EoSs, considering both equal- and unequal-mass binaries ($q = 1.38,\ 1.63$), with aligned (up to $\chi = 0.2$), anti-aligned (maximum $\chi = -0.1$), and irrotational models. They found that in cases undergoing prompt collapse to a BH, spin increases the lifetime of the remnant NS before collapse, and tends to enhance (suppress) the disc mass for aligned (anti-aligned) spin models.

Although our understanding of BNS mergers has progressed from early efforts to investigate BH formation during the inspiral phase (J. R. Wilson & G. J. Mathews 1995) to realistic simulations of spinning, magnetized mergers with detailed neutrino emission and absorption, current simulations still have simplifications that remain challenging to overcome.

In this study, we extend current spinning BNS merger studies to highly aligned, anti-aligned, and mixed spin models. We focus on the effect of varying spin on mergers of equal- and unequal-mass BNS in quasi-circular orbits. The aim is to perform state-of-the-art simulations of various spin configurations in BNS mergers and investigate whether the spin parameter can be constrained using GWs and possible EM counterparts. The centre-to-centre separation

Table 1. The ID parameters and merger times. $M_{\rm tot}^{\infty}/M_{\rm tot}^{\rm loc}$ ($\rm M_\odot$) represents the ratio of the total Arnowitt-Deser-Misner (ADM) mass computed in isolation to the total ADM mass at the initial separation. $M_{1,2}$ and $M_{1,2}^{\rm b}$ correspond to the ADM mass in isolation and the baryonic mass of each star, respectively. J_0, f_0, and $\chi_{1,2}$ represent the total angular momentum, the initial orbital frequency of the binary, and the dimensionless spin parameter of each star. The quantity $t - t_{\rm merger}$ shows the difference in inspiral time relative to the reference models. The respective reference models are marked with an asterisk (∗) for clarity. Negative (positive) values indicate shorter (longer) inspiral times compared to the reference models.

Model	$M_{\rm tot}^{\infty}/M_{\rm tot}^{\rm loc}$ ($\rm M_\odot$)	M_1 ($\rm M_\odot$)	M_2 ($\rm M_\odot$)	$M_1^{\rm b}$ ($\rm M_\odot$)	$M_2^{\rm b}$ ($\rm M_\odot$)	J_0 ($\rm M_\odot^2$)	f_0 (Hz)	χ_1	χ_2	$t - t_{\rm merger}$ (ms)	
$M255_{00}$	2.5456/2.5194	1.2728	1.2728	1.3902	1.3902	6.334 25	324	0.00	0.00	10.35(10.11)	∗
$M255_{\downarrow 0.4 0}$	2.5456/2.5273	1.2728	1.2728	1.3902	1.3902	5.811 42	326	−0.40	0.00	−5.61(−5.40)	
$M255_{\uparrow 0.4 0}$	2.5456/2.5271	1.2728	1.2728	1.3902	1.3902	6.998 39	326	0.40	0.00	+1.48(+1.39)	
$M255_{\downarrow 0.4 \downarrow 0.4}$	2.5456/2.5280	1.2728	1.2728	1.3853	1.3853	5.218 92	326	−0.40	−0.40	−6.84(−6.61)	
$M255_{\downarrow 0.4 \uparrow 0.4}$	2.5456/2.5347	1.2728	1.2728	1.3902	1.3902	6.430 15	326	−0.40	0.40	−4.85(−4.69)	
$M255_{\uparrow 0.4 \uparrow 0.4}$	2.5456/2.5272	1.2728	1.2728	1.3853	1.3853	7.590 55	326	0.40	0.40	+2.55(+2.34)	
$M255_{\downarrow 0.65 \downarrow 0.65}$	2.5456/2.5220	1.2728	1.2728	1.3701	1.3701	4.462 66	326	−0.65	−0.65	−5.42(−5.25)	
$M255_{\downarrow 0.65 \uparrow 0.65}$	2.5456/2.5130	1.2728	1.2728	1.3701	1.3701	6.386 63	326	−0.65	0.65	−2.44(−2.35)	
$M255_{\uparrow 0.67 \uparrow 0.67}$	2.5456/2.4932	1.2728	1.2728	1.3695	1.3695	8.390 40	326	0.67	0.67	−0.04(−0.77)	
$M305_{00}$	3.0500/3.0161	1.5250	1.5250	1.7028	1.7028	8.669 39	349	0.00	0.00	7.60	∗
$M305_{\downarrow 0.4 \downarrow 0.4}$	3.0500/3.0181	1.5250	1.5250	1.6883	1.6883	7.009 62	349	−0.40	−0.40	−4.33	
$M305_{\uparrow 0.4 \uparrow 0.4}$	3.0500/3.0159	1.5250	1.5250	1.6883	1.6883	10.340 24	349	0.40	0.40	+1.92	
$M305_{\uparrow 0.67 \uparrow 0.67}$	3.0500/3.0156	1.5250	1.5250	1.6687	1.6687	11.483 28	349	0.67	0.67	+0.09	
$M305q205_{00}$	3.0500/3.0201	2.0500	1.0000	2.4215	1.0670	7.649 93	348	0.00	0.00	−0.73	
$M305q205_{\uparrow 0.6 0}$	3.0500/3.0203	2.0500	1.0000	2.3391	1.0670	9.952 96	348	0.60	0.00	+0.68	
$M410_{00}$	4.1000/4.0425	2.0500	2.0500	2.4215	2.4215	14.436 15	385	0.00	0.00	4.52	∗
$M410_{\downarrow 0.65 \uparrow 0.65}$	4.1000/4.0445	2.0500	2.0500	2.3268	2.3268	14.401 56	385	−0.65	0.65	−0.82	
$M410_{\downarrow 0.65 \downarrow 0.65}$	4.1000/4.0418	2.0500	2.0500	2.3268	2.3268	9.712 22	385	−0.65	−0.65	−1.02	
$M410_{\uparrow 0.67 \uparrow 0.67}$	4.1000/4.0458	2.0500	2.0500	2.3237	2.3237	19.264 07	385	0.67	0.67	+1.99	

is primarily 40 km, except for three test models, where it is 60 km. We use the finite-temperature, composition-dependent Steiner–Fischer–Hempel EoS with parameter set 'o' (SFHo; A. W. Steiner, M. Hempel & T. Fischer 2013) and account for neutrino emission and absorption. We consider three total mass configurations, where the equal-mass irrotational models result in long-lived NS, or prompt BH formation. This paper is organized as follows: Section 2 outlines the ID and the numerical methods; Section 3 details the analysis methods; the results for models with $M_{\rm tot} = 2.55$ $\rm M_\odot$ are presented in Section 4, while results for models with $M_{\rm tot} = 3.05$ and 4.10 $\rm M_\odot$ are presented in Section 5; the discussion and conclusion are given in Section 6. Geometrized units ($G = c = 1$) are used unless otherwise specified.

2 NUMERICAL SET-UP

The ID for all BNS models is created using the Fuka branch of the Kadath library (P. Grandclement 2010; L. J. Papenfort et al. 2021). Table 1 summarizes the ID parameters and the corresponding merger times.

General relativistic hydrodynamics (GRHD) evolution is performed using WHISKYTHC (D. Radice & L. Rezzolla 2012; D. Radice, L. Rezzolla & F. Galeazzi 2014a, b, 2015), a finite-difference/finite-volume High-Resolution Shock-Capturing (HRSC) code that implements the Valencia formulation of the general relativistic hydrodynamics equations (F. Banyuls et al. 1997).Built on the `Cactus` framework (G. Allen et al. 1999; T. Goodale et al. 2003; Cactus developers 2023a, b), WHISKYTHC employs the `Carpet` adaptive mesh refinement driver (E. Schnetter, S. H. Hawley & I. Hawke 2004). NSs are modelled as perfect fluids, with the energy-momentum tensor given as (D. Radice & L. Rezzolla 2012; D. Radice et al. 2014a, b, 2015)

$$T^{ab}_{\rm h} = \rho h u^a u^b + p g^{ab}, \tag{1}$$

where ρ is the rest-mass density, $h = 1 + \epsilon + p/\rho$ is the specific enthalpy, with ϵ the specific internal energy, p is the pressure, u^a is the fluid four-velocity, g^{ab} is the metric tensor, and $T^{ab}_{\rm h}$ is the energy-momentum tensor for pure hydrodynamics. For our systems, the atmosphere density and temperature are set to $\rho = 6.176 \times 10^3$ g cm^{-3} and $T = 0.02$ MeV. The conservation of total energy-momentum, including neutrinos, is given by $\nabla_b T^{ab}_{\rm rad} = Q u^b$, where Q is the net energy deposition rate due to the absorption and emission of the neutrinos (D. Radice et al. 2018b). We use the finite-volume HRSC method, which employs a fifth-order monotonicity-preserving scheme (MP5; A. Suresh & H. T. Huynh 1997) for reconstruction and the Harten–Lax–van Leer–Einfeldt Riemann solver (B. Einfeldt 1988) for flux calculation. Neutrinos are included using M0 + Leakage (D. Radice et al. 2016b), which tracks electron neutrinos, $\nu_{\rm e}$, anti-electron neutrinos, $\bar{\nu}_{\rm e}$, and heavy-lepton neutrinos, ν_x; the latter denotes the collective group of the muon and tau neutrino and anti-neutrinos. The emission from the optically thick regions is computed via a gray leakage scheme, while the transport and radial propagation in optically thin regions is handled by the M0 scheme over a spherical grid (see D. Radice et al. 2016b for the detailed explanation of the neutrino treatment). The average energy and luminosity of free-streaming neutrinos is calculated on a uniform spherical grid with radius ∼756 km and size $(r, \theta, \phi) = (3096, 32, 64)$, using 2048 rays. We use the finite-temperature, composition-dependent SFHo EoS (A. W. Steiner et al. 2013), which is considered soft as it yields for a typical NS with mass $M = 1.4$ $\rm M_\odot$ and radius of ∼11.9 km. The EoS is fully hadronic, and is available on Stellarcollapse (2017) and E. O'Connor & C. D. Ott (2010).

Space–time evolution is performed with CTGAMMA (D. Pollney et al. 2011), which is based on the publicly available software platform `Einstein Toolkit` (F. Löffler et al. 2012; M. Zilhão & F. Löffler 2013; R. Haas et al. 2022; The Einstein Toolkit 2025). We use the constraint damping Z4c formulation of the Einstein field

equations by S. Bernuzzi & D. Hilditch (2010), which is used within CTGAMMA, with moving puncture gauge conditions. The comparison of Z4c and Baumgarte–Shapiro–Shibata–Nakamura–Oohara–Kojima (BSSNOK) formulations (T. Nakamura, K. Oohara & Y. Kojima 1987; M. Shibata & T. Nakamura 1995; T. W. Baumgarte & S. L. Shapiro 1998) shows that the former has a substantially lower constraint violation, more accurate GW phase, and amplitude (A. Weyhausen, S. Bernuzzi & D. Hilditch 2012; D. Hilditch et al. 2013, and references therein). The coupling between space–time and GRHD variables is handled by the `Method of Lines (MoL)`. We use the strong stability preserving third-order Runge–Kutta method (S. Gottlieb, D. I. Ketcheson & C.-W. Shu 2009; D. Radice 2020) for time integration. The time-step factor is chosen according to the Courant–Friedrichs–Lewy `(CFL)` condition to be 0.15.

We use a cell-centred grid structure extending to ≈2835 km in all three directions, with reflection symmetry applied along the z-axis to reduce the computational cost. We use seven refinement levels, the finest grid of which has a resolution of ≈308 m, which is denoted as LR, low resolution, for all cases, except for $M_{\rm tot} = 2.55\ {\rm M}_\odot$ models, which are also simulated with a resolution of ≈222 m, denoted as HR, high resolution. The '`Sophie Kowalevski`' release of the `Einstein Toolkit` (R. Haas et al. 2022) is used.

3 ANALYSIS METHODS

We perform post-processing using `PostCactus` (W. Kastaun 2021) and `Scidata` (D. Radice 2023). Unless otherwise stated, the presented plots and figures are based on LR simulations.

Naming and resolution: Models are named based on total mass, mass ratio for unequal-mass models, and spins. For example, $M255_{00}$ refers to an equal-mass, irrotational model with $M_{\rm tot} = 2.55\ {\rm M}_\odot$, while $M305q205_{\uparrow 0.6 0}$ represents an unequal-mass model, $q = 2.05$, with the primary component having an aligned spin of $\chi_1 = 0.6$ relative to the orbital angular momentum, and the secondary being irrotational, with a total mass of $3.05\ {\rm M}_\odot$.

Merger time ($t_{\rm merger}$): Merger times are determined as being the time of maximum GW amplitude, measured by a detector placed at ≈295 km.

Final time: For models resulting in an NS, comparisons are made at ≈20 ms after the merger, while for models forming a BH, comparisons are made at ≈10 ms after the merger.

Spins: Unless otherwise specified, spins refer to the effective spin of the binary. Orientations, such as aligned or anti-aligned, are defined relative to the orbital angular momentum $\boldsymbol{L}$. We use the following conventions:

(i) **irrotational** (00), where both stars are irrotational;
(ii) **aligned** (↑↑), or **anti-aligned** (↓↓), where both spins are aligned (anti-aligned) with $\boldsymbol{L}$;
(iii) **single-spin aligned** (↑ 0), or **single-spin anti-aligned** (↓ 0), where the primary has aligned (anti-aligned) spin while the secondary is irrotational; and
(iv) **mixed** (↓↑), where the primary has anti-aligned and the secondary has aligned spins.

Neutrinos: The $M0$ + Leakage scheme described in Section 2 is used to calculate the effect of spin on the average neutrino energies and luminosities for electron neutrinos, $\nu_{\rm e}$, electron anti-neutrino, $\overline{\nu}_{\rm e}$, and heavy-lepton neutrinos, ν_x. Neutrino quantities are extracted at the outer boundary of the spherical grid.

GWs: GWs are computed using the `WeylScal4` and `Multipole` thorns of the `Einstein Toolkit`. The `WeylScal4` thorn calculates the Newman–Penrose curvature scalar Ψ_4, while the `Multipole` thorn decomposes Ψ_4 into $s = -2$ spin-weighted spherical harmonic modes on a sphere with a radius of ≈295 km. The strain is computed from the double time integration of Ψ_4 using fixed frequency integration (C. Reisswig & D. Pollney 2011)

$$h = h_+^{lm}(r,t) - i h_\times^{lm}(r,t) = \int_{-\infty}^{t} {\rm d}u \int_{-\infty}^{u} {\rm d}v\ \Psi_4^{lm}(r,v), \tag{2}$$

where h_+ and $h_\times$ represent the plus '+' and cross '×' polarization of the GWs. The quantity Ψ_4 is given as

$$\Psi_4(t,r,\theta,\phi) = \sum_{l=2}^{l=8} \sum_{m=-l}^{l} \Psi_4^{lm}(t,r)\, {}_{-2}Y_{lm}(\theta,\phi). \tag{3}$$

The peak GW frequencies for a given (l, m) mode correspond to the frequencies of the peak effective strain, $h_{\rm eff} = \sqrt{h_+^2 + h_\times^2}$. We look at energy and angular momentum loss (in $+z$ direction), frequencies and spectra of the GWs, and consider modes up to $(l, m) = (8, 8)$. We also discuss their detectability at a distance of 100 Mpc by the Advanced LIGO (The LIGO Scientific Collaboration 2015; LIGO Collaboration 2022) and the Einstein Telescope (ET; S. Hild et al. 2011; M. Maggiore et al. 2020). The instantaneous frequency at the moment of merger, $f_{\rm merger}$, and the post-merger peak frequencies, where f_1, f_2, and f_3 correspond to $(l, m) = (2, 1)$, $(2, 2)$, and $(3, 3)$ modes, respectively, are also presented. Among them, the f_2 frequency has been shown to correlate strongly with the radius of the maximum TOV mass, providing a direct insight into the underlying EoS (A. Bauswein & H. T. Janka 2012; A. Bauswein, T. W. Baumgarte & H. T. Janka 2013; A. Bauswein, N. Stergioulas & H.-T. Janka 2016).

Ejecta: Ejecta properties, representing unbound matter that does not fall back, are calculated from a surface located at ∼295 km. The geodesic criterion (T. Dietrich et al. 2015a; W. Kastaun & F. Galeazzi 2015; Y. Sekiguchi et al. 2015; D. Radice et al. 2016b) $u_t < -1$, where u_t is the time component of the four-velocity, is used. We also analyse the fast-moving component of the neutron-rich ejecta with velocity greater than $0.6c$, which is expected to yield synchrotron radiation via interaction with the interstellar medium (K. Hotokezaka et al. 2018; D. Radice et al. 2018b). The electron fraction and velocity of the matter are given as mass-weighted averages.

Remnant properties: The apparent horizon of a BH is detected with `AHFinderDirect` (J. Thornburg 1996, 2004; J. D. Brown et al. 2009). The (quasi-local) spin and mass measurement of a BH are performed using `QuasiLocalMeasures` (O. Dreyer et al. 2003). Following N. Tacik et al. (2015), we compute the quasi-local angular momentum from six spherical surfaces centred at the coordinate origin. Five of these surfaces are located at radii ranging from ≈1.48 to ≈16 km, where the latter approximately corresponds to the size of NS remnants. The sixth surface is placed further out, at a radius of ≈29.5 km.

Disc mass: The baryonic mass of the disc is calculated by integrating the mass within a rest-mass density threshold of $\rho < 10^{13}\ {\rm g\,cm^{-3}}$ over a radius of ≈295 km, similarly to D. Radice et al. (2018b) and references therein, and see also A. Camilletti et al. (2024). If a BH is formed, we remove the region with lapse function values lower than 0.3.

4 RESULTS FOR MODELS WITH $M_{\rm tot} = 2.55\ {\rm M}_\odot$

We focus our analysis on the models with $M_{\rm tot} = 2.55\ {\rm M}_\odot$ and leave other models to Section 5, to improve readability.

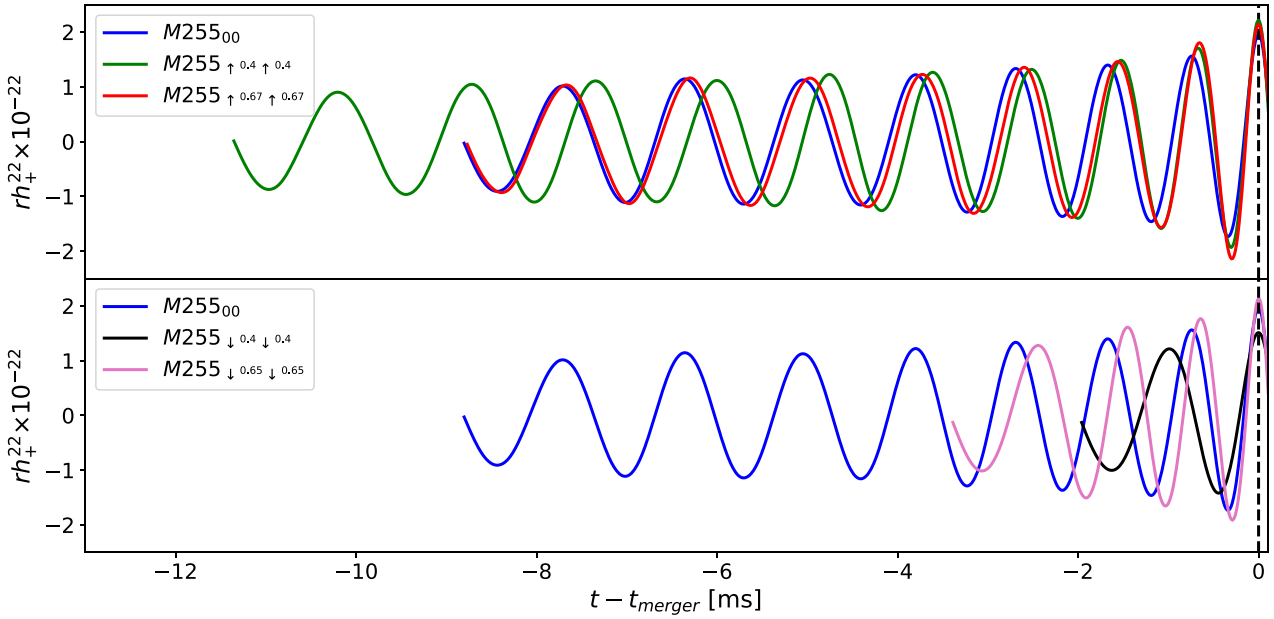

Figure 1. GW strains for aligned (top panel) and anti-aligned (bottom panel) spin models, shown up to 0.1 ms after the merger from HR simulations. The strains are aligned at the merger time (vertical dashed line), with the change in trend with spin distinctly visible in both panels: note differences in merger times.

This section investigates the effect of initial spin on the dynamics by analysing the inspiral times, listed in Table 1, and identifying possible mechanisms responsible for observed differences and variations.

Impact of spin on the inspiral phase: As discussed in Section 1, previous studies have shown that spin–orbit interaction is repulsive, resulting in delay of merger, for aligned spins and attractive for anti-aligned spins, producing a speed-up of merger. Our simulations, however, reveal a change of this qualitative trend. It arises probably from the interplay between spin–orbit and spin–spin interactions, for spins in the range of $\chi = 0.4{-}0.67$ in both aligned and anti-aligned models. In this regime, increasing the spin decreases inspiral time for aligned spins; and vice versa for anti-aligned spins, inspiral time increases. The single-spin models have only $|\chi_1| = 0.4$ and hence are outwith the parameter range. These follow the general trend of previous studies.

The mixed spin models further illustrate the importance of individual spins for the inspiral time. Despite having $\chi = 0$, $M255_{\downarrow 0.4 \uparrow 0.4}$ and $M255_{\downarrow 0.65 \uparrow 0.65}$ merge ∼4.9 and ∼2.4 ms earlier than the irrotational model. Increasing the individual spin from $|\chi_{1,2}| = 0.4$ to 0.65 therefore shortens the inspiral, consistent with the change in trend observed in aligned and anti-aligned models.

Since the equatorial bulge increases with spin, two aligned spin models, $M255_{\uparrow 0.4 \uparrow 0.4}$ and $M255_{\uparrow 0.67 \uparrow 0.67}$, are simulated with a larger initial separation of ∼60 km. These models are not included in any analysis and do not appear in any figure or table. They serve solely as a robustness check, confirming that the observed change in trend is independent of the initial separation. They exhibit a similar trend regarding the time spent in the inspiral phase as compared to other models, allowing us to rule out any significant impact of the initial separation on the observed change in trend with spin.

A similar change in trend is identified for anti-aligned spins between $M255_{\downarrow 0.4 \downarrow 0.4}$ and $M255_{\downarrow 0.65 \downarrow 0.65}$. Although our simulations for larger separation are focused on aligned spins, we hypothesize that this behaviour in anti-aligned spins follows the same underlying mechanism, the interplay between spin–orbit and spin–spin interactions. To support this interpretation, Fig. 1 presents the GW strain until 0.1 ms after the merger for both aligned and anti-aligned spins alongside the irrotational model. The figure highlights the change in trend across different spin configurations.

For moderate spins of $\chi = 0.4$, spin–orbit interaction largely dominates the dynamics, leading to a longer inspiral phase. However, as the spin increases beyond $\chi = 0.4$ spin–spin effects become increasingly important, counteracting the spin–orbit interactions (T. Dietrich et al. 2017b), causing earlier (later) mergers despite higher spin for aligned (anti-aligned) spins. While this behaviour is observed consistently at both low and high resolutions (see Table 1), we note that its robustness at even higher resolutions may require further confirmation.

Evolution of thermodynamic properties: We now show the impact of the spin effects and differences on the maximum rest-mass density and temperature of the matter.

For models with spins up to $|\chi| = 0.4$, aligned (anti-aligned) spins result in a longer (shorter) inspiral phase and less (more) violent mergers, as evidenced by reaching lower (higher) maximum temperatures and rest-mass densities as compared to the irrotational model. For higher spins, such as $M255_{\downarrow 0.65 \downarrow 0.65}$ and $M255_{\uparrow 0.67 \uparrow 0.67}$, despite the change in trend observed in orbital dynamics, the overall trend remains consistent: increasing aligned (anti-aligned) spin continues to produce less (more) violent mergers. The values of maximum temperatures and rest-mass densities change with spin peaking at ∼145 MeV and $\sim 5.6\rho_{\rm sat}$ for the $M255_{\downarrow 0.65 \downarrow 0.65}$ model, where $\rho_{\rm sat}$ is the nuclear saturation density of 2.7×10^{14} g cm^{-3} (J. M. Lattimer 2012). This suggests that for spins above $|\chi| = 0.4$, where both spin–orbit and spin–spin interactions significantly influence the dynamics, merger intensity cannot be solely determined by the timing of the merger.

Snapshots of the temperature of the remnant and of the composition of the disc, along with the rest-mass density contours, at 20 ms after the merger, are shown in Fig. 2 and in Fig. 3, respectively. These figures illustrate that in aligned (and single-spin aligned) models the additional angular momentum increases the rotational support of

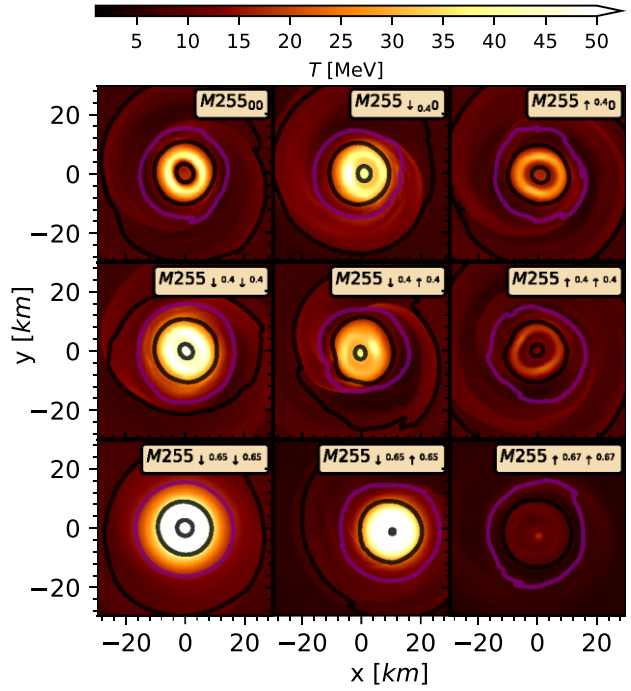

Figure 2. The temperature distribution of the remnant and the inner disc region is shown for $M_{\rm tot} = 2.55\ {\rm M}_{\odot}$ at 20 ms after the merger in the x–y plane. The purple contour marks a rest-mass density of $\rho = 10^{13}\ {\rm g\,cm^{-3}}$, and black contours denote $\rho = 10^{12}$, 10^{14}, and $10^{15}\ {\rm g\,cm^{-3}}$. Panels represent the different spin configurations, illustrating the impact of spin on the temperature structure of the remnant.

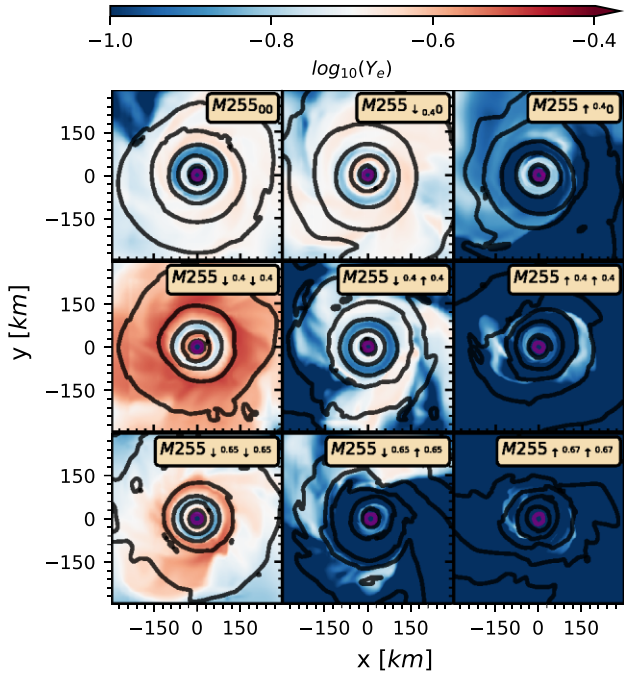

Figure 3. The distribution of electron fraction $Y_{\rm e}$ in the remnant and disc is shown at 20 ms after the merger. Both $Y_{\rm e}$ and the rest-mass density contours are presented on logarithmic scales, with black contours marking densities of $\rho = 10^{6}$, 10^{7}, 10^{8}, 10^{9}, 10^{10}, 10^{11}, and $10^{12}\ {\rm g\,cm^{-3}}$, and the purple contour representing $\rho = 10^{13}\ {\rm g\,cm^{-3}}$. This figure highlights the impact of spin on the composition.

the remnant, making it less compact and reducing shock heating, which results in a cooler core surrounded by a hot envelope with the maximum densities reached more gradually, following the same pattern as the irrotational model. The redistribution of the additional angular momentum leads to the formation of spiral arms, the strength of which increases with spin. At 20 ms after the merger, only part of the remnant of these arms are visible for the aligned spin model $M255_{\uparrow 0.67 \uparrow 0.67}$.

In contrast, for anti-aligned (including single-spin anti-aligned) models, the reduced angular momentum weakens the rotational support of the remnant, leading to a more compact and hotter remnant with densities peaking almost immediately after the merger. In mixed spin models, enhanced spin–spin interaction results in a more violent merger. It leads to strong shock heating and a uniformly hot core for $M255_{\downarrow 0.65 \uparrow 0.65}$ and a hotter core than irrotational model despite weaker heating for $M255_{\downarrow 0.4 \uparrow 0.4}$. These features are illustrated in Fig. 2.

In the single-spin models, $M255_{\downarrow 0.40}$, and $M255_{\uparrow 0.40}$, the spinning NSs become tidally disrupted, due to larger equatorial bulge, but in the aligned spin model the tidal tail is more pronounced due to the additional angular momentum. Looking at the impact of spin on the compositional change of the disc, we see in Fig. 3 that the mixed spin model, $M255_{\downarrow 0.65 \uparrow 0.65}$, still retains a tidal stream, which is mainly composed of neutrons. In general, anti-aligned (aligned) spins result in less (more) neutron-rich discs compared to the irrotational models. This trend can be attributed to the impact of weak interactions, which are discussed in the following section.

Neutrinos: Neutrinos play a crucial role in determining the composition of matter through weak interactions and influence the stability and thermodynamic properties of the remnant NS by carrying energy away. They also drive the ejecta to higher altitudes (larger $|z|$ values) and affect its composition (D. Radice et al. 2018b). These quantities, along with the mass and velocity of the ejecta, determine r-process nucleosynthesis and properties of the ensuing kilonovae. See D. Radice et al. (2018b) and P. L. Espino et al. (2024) for the impact of neutrinos on the ejecta and F. Foucart (2023) for a recent review of the impact of neutrinos in BNS mergers.

Using the M0 + Leakage scheme, details of which can be reviewed in Section 2, we now discuss the impact of initial spin on average neutrino energies and luminosities for the electron neutrino ($\nu_{\rm e}$), electron anti-neutrino ($\overline{\nu}_{\rm e}$), and the heavy-lepton neutrinos (ν_x), as presented in Fig. 4. This figure enables a direct comparison of mean energies and luminosities for all flavours, covering aligned and anti-aligned spin configurations as well as the irrotational model. In all models, the flavour hierarchy remains consistent: $\langle E_{\nu_x} \rangle > \langle E_{\overline{\nu}_{\rm e}} \rangle > \langle E_{\nu_{\rm e}} \rangle$ and this does not change across any spin configurations considered here. This ordering is consistent with F. Foucart et al. (2016), D. Radice et al. (2022), and D. Radice & S. Bernuzzi (2023).

In contrast, the luminosity hierarchy varies with spin. Anti-aligned models produce compact, hot remnants that enhance heavy-lepton neutrino emission, resulting in a hierarchy of $L_{\nu_x} > L_{\overline{\nu}_{\rm e}} > L_{\nu_{\rm e}}$, similar to the irrotational and single-spin anti-aligned model. Despite being less compact than these models, and experiencing stronger shock heating than the irrotational model, the mixed spin model $M255_{\downarrow 0.65 \uparrow 0.65}$ also exhibits the same hierarchy. Here, L_{ν_x} denotes the total luminosity of the heavy-lepton neutrinos, the sum over ν_μ, $\overline{\nu}_\mu$, ν_τ, and $\overline{\nu}_\tau$.

Aligned spin models, by contrast, yield more extended and dilute remnants with lower temperature, which suppress the overall neutrino number flux. In these models, the dominant emission shifts to electron anti-neutrinos, leading to a luminosity hierarchy of $L_{\overline{\nu}_{\rm e}} > L_{\nu_{\rm e}} > L_{\nu_x}$. On the other hand, single-spin aligned and mixed

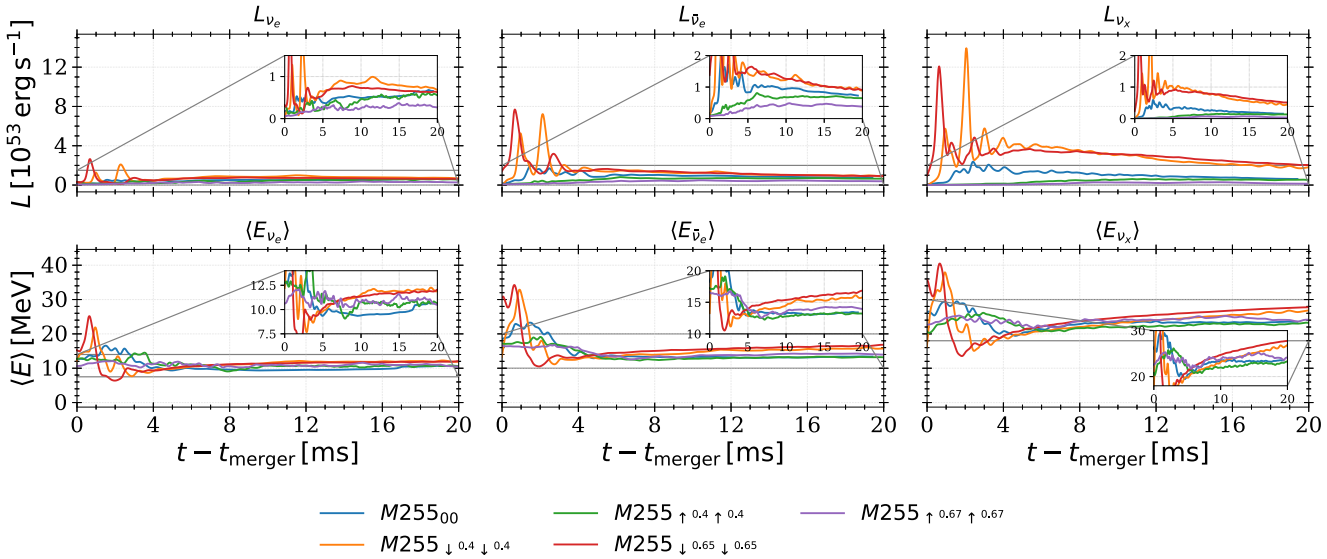

Figure 4. Neutrino luminosities and mean energies for electron neutrinos (ν_e), electron anti-neutrinos ($\bar{\nu}_e$), and heavy-lepton neutrinos (ν_x) for $M_{\mathrm{tot}} = 2.55\,\mathrm{M}_\odot$ models with different spins. Anti-aligned spins yield higher mean energies and enhanced luminosities than the aligned spins due to higher neutrino number flux from more compact and hotter remnants. Main panels share a common y-axis to illustrate overall trends, whereas inset panels use their own scales to enhance visualization of temporal variations.

spin model $M255_{\downarrow 0.4\uparrow 0.4}$ show enhanced ν_x relative to ν_e leading to the hierarchy of $L_{\bar{\nu}_e} > L_{\nu_x} > L_{\nu_e}$.

These results highlight that spin orientation strongly affects the morphology and thermal properties of the remnant, which in turn shapes the neutrino emission properties.

GW*s*: The impact of spin on GW emission is analysed by examining the total extracted energy and angular momentum loss, their relative contributions during the inspiral phase, and the ratio of total energy and angular momentum release to the initial values for mass-energy and angular momentum. In Table 2, we summarize these quantities, along with the merger and peak frequencies of modes contributing more than 2×10^{-3} to the total energy release. We stress that GW quantities during the inspiral phase are meaningful only within the context of an initial separation of 40 km, and do not represent absolute physical differences across models.

Models with aligned spins radiate more energy and angular momentum than anti-aligned spin models with the same spin magnitude, while the irrotational model exhibits the highest overall energy and angular momentum release. The GW strains, shown in Fig. 1, clearly demonstrate the impact of spin on the dynamics. During the post-merger phase (not shown in Fig. 1), spin magnitude and orientation significantly influence the remnant oscillation, mimicking the effects of softer or stiffer EoS or unequal-mass binaries. GW radiation efficiency decreases with increasing anti-aligned spin due to the formation of a more compact remnant. Conversely, aligned spins lead to less compact remnants with extended spiral arms, enhancing the radiation efficiency. Single-spin models follow the aligned (anti-aligned) models, with differences in energy and angular momentum radiation and frequency shifts in f_1 and f_2 remaining within the estimated numerical uncertainties, and thus not indicative of new behaviour, while $M255_{\downarrow 0.65\uparrow 0.65}$ model shows the lowest energy emission through GWs.

In Figs 5 and 6, we show the GW spectra for the (2, 1) and (2, 2) modes, along with the sensitivity curves of Advanced LIGO and the ET. We observe that the peak frequency of the fundamental mode f_2, shifts to higher frequencies for aligned spins, consistent with T. Dietrich et al. (2017b), but in contrast to S. Bernuzzi et al. (2014), W. E. East et al. (2019), and S. Rosswog et al. (2024). For anti-aligned spins, the frequency shift is more pronounced, with the largest difference compared to the irrotational model being ∼0.39 kHz for $M255_{\downarrow 0.65\,\downarrow 0.65}$. These shifts are larger than the estimated numerical uncertainties, which we obtain by comparing HR and LR values with $\Delta f = |f_{\mathrm{HR}} - f_{\mathrm{LR}}|$, at most $\Delta f_2 \lesssim 0.18$ kHz. Shifting to the lower frequencies for the anti-aligned spins contrasts with W. E. East et al. (2019), who considered $\chi = -0.13$, likely due to the higher spins, $\chi = -0.4$ and $\chi = -0.65$, analysed in this study. These shifts in the f_2 demonstrate that spins, particularly high spins (both aligned and anti-aligned), can introduce degeneracies in the GW spectra, complicating the inference of the EoS. A shift to lower (higher) frequencies mimics the effects of a stiffer (softer) EoS, compared to the irrotational model. Unlike f_2 frequencies, the (2, 1) mode, associated with the one-arm spiral instability, shows shifts within numerical uncertainties, found to be at most $\Delta f_1 \lesssim 0.08$ kHz, except for $M255_{\downarrow 0.65\,\downarrow 0.65}$, where the difference reaches ∼1.23 kHz.

Ejecta: In Table 3, we summarize the properties of the ejected matter, including total mass, fast-moving ejecta mass, velocity, and electron fraction. Across all spin configurations, the total ejecta mass increases compared to the irrotational model, with aligned spins producing a higher total ejecta mass than the anti-aligned spins. Single-spin models yield ejecta masses broadly consistent with aligned (anti-aligned) models, while the mixed spin model $M255_{\downarrow 0.65\uparrow 0.65}$ produces an ejecta mass comparable to that of the $M255_{\uparrow 0.67\uparrow 0.67}$ model, both give ∼0.06 $\mathrm{M}_\odot$.

The composition shows a clear dependence of spin orientation: anti-aligned spins generally result in less neutron-rich ejecta compared to the aligned spins.

The mass of the fast-moving ejecta, as defined in Section 3, lies between 10^{-8} and $10^{-4}\,\mathrm{M}_\odot$, and depends on the EoS, as demonstrated in D. Radice et al. (2018b). Specifically, binaries with SFHo EoS were shown to exhibit fast-moving ejecta not only during the merger, but

Table 2. Energy and angular momentum radiated by GWs, along with merger and peak frequencies, of modes contributing more than 2×10^{-3} to the total energy release. $E^{\rm gw}_{\rm ins}$ ($J^{\rm gw}_{\rm ins}$), $E^{\rm gw}_{\rm tot}$ ($J^{\rm gw}_{\rm tot}$), and $E^{\rm gw}_{\rm tot}/M^{\rm loc}_{\rm tot}$ ($J^{\rm gw}_{\rm tot}/J_0$) show energy (angular momentum) loss during inspiral, the total energy (angular momentum) loss, and the ratio of the total energy (angular momentum) loss to the total initial mass energy (angular momentum), respectively. Additionally, $f_{\rm merger}$ denotes the instantaneous frequency at the merger time, while f_1, f_2, and f_3 represent the peak frequencies corresponding to the $(l, m) = (2, 1)$, $(2, 2)$, and $(3, 3)$ modes, respectively. For remnants undergoing prompt collapse to a BH, only $f_{\rm merger}$ is provided. When parentheses are present, the values in parentheses correspond to LR simulations, while non-parenthesized values represent HR simulations.

Model	$E^{\rm gw}_{\rm ins}$ (per cent)	$E^{\rm gw}_{\rm tot}$ ($\times 10^{52}$ erg)	$E^{\rm gw}_{\rm tot}/M^{\rm loc}_{\rm tot}$ ($\times 10^{-2}$)	$J^{\rm gw}_{\rm ins}$ (per cent)	$J^{\rm gw}_{\rm tot}$ ($M^2_\odot$)	$J^{\rm gw}_{\rm tot}/J_0$ ($\times 10^{-2}$)	$f_{\rm merger}$ (kHz)	f_1 (kHz)	f_2 (kHz)	f_3 (kHz)
$M255_{00}$	20(22)	9.18(9.64)	2.04(2.14)	42(43)	1.59(1.64)	25.17(25.83)	1.70(2.08)	1.46(1.54)	2.89(2.93)	4.35(4.34)
$M255_{\downarrow 0.4 0}$	8(12)	8.45(5.45)	1.87(1.21)	19(27)	1.25(0.86)	21.50(14.88)	1.34(1.41)	1.46(1.48)	2.91(2.99)	4.26(4.32)
$M255_{\uparrow 0.4 0}$	23(24)	8.54(9.49)	1.89(2.10)	46(46)	1.58(1.68)	22.61(23.97)	1.62(2.03)	1.51(1.53)	3.03(2.97)	4.38(4.44)
$M255_{\downarrow 0.4 \downarrow 0.4}$	14(9)	3.16(5.03)	0.70(1.11)	29(19)	0.54(0.80)	10.39(15.32)	1.32(1.34)	1.46(1.44)	2.80(2.69)	4.14(4.05)
$M255_{\downarrow 0.4 \uparrow 0.4}$	27(17)	4.68(7.68)	1.03(1.69)	46(33)	0.83(1.16)	12.85(18.03)	2.09(2.23)	1.48(1.54)	2.86(3.04)	4.24(4.51)
$M255_{\uparrow 0.4 \uparrow 0.4}$	32(39)	7.74(7.60)	1.71(1.68)	55(61)	1.55(1.49)	20.39(19.67)	1.90(2.38)	1.47(1.49)	3.01(2.97)	4.51(4.54)
$M255_{\downarrow 0.65 \downarrow 0.65}$	30(38)	5.80(4.83)	1.29(1.07)	45(56)	1.09(0.89)	24.32(19.95)	2.01(2.24)	2.54(1.21)	2.50(2.56)	2.54(3.73)
$M255_{\downarrow 0.65 \uparrow 0.65}$	67(72)	2.31(2.32)	0.51(0.52)	77(82)	0.70(0.68)	10.95(10.67)	1.56(1.75)	2.58(2.53)	2.62(2.53)	2.55(2.56)
$M255_{\uparrow 0.67 \uparrow 0.67}$	69(51)	3.35(3.33)	0.75(0.75)	83(68)	0.92(0.90)	11.01(10.72)	1.93(1.55)	1.49(1.48)	3.00(2.96)	4.22(4.33)
$M305_{00}$	57	5.50	1.02	75	1.34	15.46	1.94	–	–	–
$M305_{\downarrow 0.4 \downarrow 0.4}$	26	3.89	0.72	50	0.64	9.07	1.66	–	–	
$M305_{\uparrow 0.4 \uparrow 0.4}$	39	13.87	2.57	63	2.32	22.48	2.70	3.88	3.60	5.08
$M305_{\uparrow 0.67 \uparrow 0.67}$	62	5.29	0.98	76	1.38	11.99	1.87	1.68	3.14	4.61
$M305q205_{00}$	69	2.27	0.42	77	0.74	9.74	1.24	–	–	–
$M305q205_{\uparrow 0.6 0}$	60	2.80	0.52	75	0.85	8.53	1.39	3.68	3.58	5.23
$M410_{00}$	64	19.47	2.69	79	3.31	22.93	3.17	–	–	–
$M410_{\downarrow 0.65 \downarrow 0.65}$	59	11.01	1.52	73	1.82	18.78	2.96	–	–	–
$M410_{\downarrow 0.65 \uparrow 0.65}$	63	13.92	1.93	76	2.54	17.62	2.77	–	–	–
$M410_{\uparrow 0.67 \uparrow 0.67}$	75	16.04	2.22	85	3.43	17.83	2.66	–	–	–

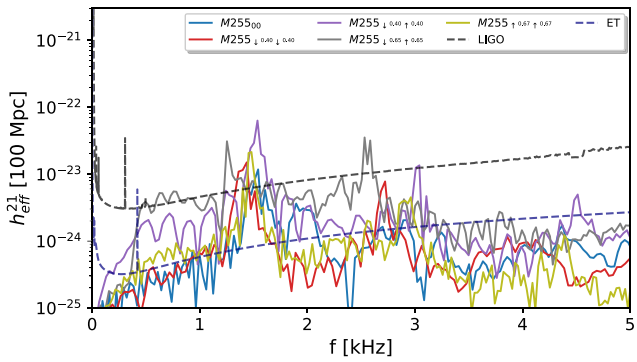

Figure 5. GW spectra for mode $(l, m) = (2, 1)$ for models with $M_{\rm tot} = 2.55\ {\rm M}_\odot$ showing their detectability by the Advanced LIGO and the ET. The dotted lines indicate the sensitivity curves of the detectors (S. Hild et al. 2011; LIGO Collaboration 2022).

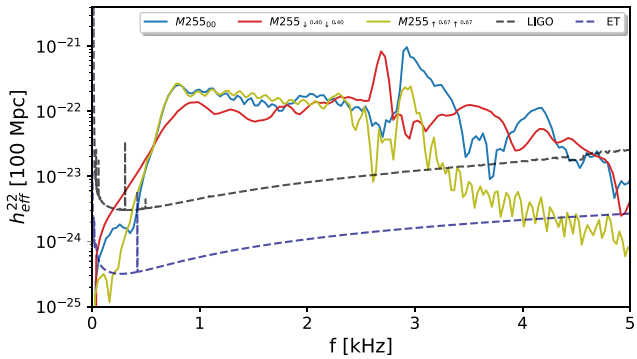

Figure 6. A similar presentation as in Fig. 5 but for the fundamental mode, $(l, m) = (2, 2)$, focusing on highly aligned, anti-aligned spin and irrotational models.

also after the first bounce of the remnant, a behaviour unique among the EoSs considered. In our study, we observe fast-moving ejecta in the anti-aligned spin models (including single-spin anti-aligned), driven by the strong shock heating, which is notably absent in the aligned spin models, and is strongly suppressed in the mixed spin models. The calculated fast-moving ejecta masses align with those reported in D. Radice et al. (2018b).

Remnants: All remnants with $M_{\rm tot} = 2.55\ {\rm M}_\odot$ result in long-lived NSs. The rotation pattern of the BNS remnants differs from single, differentially rotating NS, where the core rotates faster than the envelope. In contrast, BNS merger remnants exhibit an inverse rotation pattern, where the core rotates more slowly than the envelope (M. Shibata & K. Taniguchi 2006; W. Kastaun, R. Ciolfi & B. Giacomazzo 2016; W. E. East et al. 2019). This behaviour is illustrated in Fig. 7, which shows the variation of the dimensionless spin parameter of the long-lived NS across different radii.

Among all models, the highest spin is observed in the irrotational model, with $\chi_{\rm rem} = 0.24$. While this may initially appear counter-intuitive, it is a direct consequence of angular momentum dynamics. As shown in Table 1, anti-aligned spin models begin with significantly lower total angular momentum (J_0) because the spin vectors are oriented in the opposite direction to the orbital angular momentum and therefore reduce the total angular momentum through spin–orbit interactions. These models also produce slightly more massive remnants, contributing to a further reduction in spin. In contrast, aligned spins start with higher J_0. However, during the merger, the formation of extended spiral arms leads to a broader redistribution of angular momentum. Consequently, a smaller fraction of the initial angular momentum is retained in the remnant where the spin is measured, resulting in a lower spin despite the higher J_0.

Aligned spins also produce remnants with lower rest-mass densities and more extended structures, whereas anti-aligned models

Table 3. The ejecta properties and disc masses at final times; see Section 3 for details. The ejecta properties are extracted at a distance of $r = 295$ km. $M_{\rm ej}$ and $M_{\rm ej} \geq 0.6c$ denote the mass of total ejecta, and of fast-moving ejecta, respectively. $M_{\rm disc}$ represents the disc mass; $\langle v \rangle$ and $\langle Y_{\rm e} \rangle$ correspond to the mass-weighted average velocity and electron fraction, respectively. When parentheses are present, the values in parentheses correspond to LR simulations, while non-parenthesized values represent HR simulations.

Model	$M_{\rm ej}$ (10^{-3} M$_\odot$)	$M_{\rm ej} \geq 0.6c$ (10^{-5} M$_\odot$)	$M_{\rm disc}$ (10^{-2} M$_\odot$)	$\langle Y_{\rm e} \rangle$	$\langle v \rangle$ (c)
$M255_{00}$	1.83 (1.24)	0.05 (0.00)	24 (19)	0.32 (0.33)	0.21 (0.21)
$M255_{\downarrow 0.4 0}$	3.73 (6.86)	0.69 (2.72)	14 (21)	0.31 (0.31)	0.22 (0.22)
$M255_{\uparrow 0.4 0}$	2.25 (2.93)	0.00 (0.00)	16 (29)	0.31 (0.41)	0.22 (0.22)
$M255_{\downarrow 0.4 \downarrow 0.4}$	6.64 (11.64)	8.40 (17.36)	16 (13)	0.24 (0.25)	0.23 (0.24)
$M255_{\downarrow 0.4 \uparrow 0.4}$	2.33 (3.65)	0.06 (0.58)	22 (16)	0.32 (0.30)	0.22 (0.22)
$M255_{\uparrow 0.4 \uparrow 0.4}$	11.27 (14.59)	0.00 (0.00)	38 (37)	0.27 (0.56)	0.24 (0.23)
$M255_{\downarrow 0.65 \downarrow 0.65}$	17.01 (11.78)	28.42 (42.64)	22 (18)	0.21 (0.19)	0.24 (0.24)
$M255_{\downarrow 0.65 \uparrow 0.65}$	57.33 (55.45)	0.00 (0.11)	20 (23)	0.30 (0.32)	0.21 (0.21)
$M255_{\uparrow 0.67 \uparrow 0.67}$	58.73 (54.85)	0.00 (0.00)	28 (28)	0.29 (0.37)	0.22 (0.21)
$M305_{00}$	0.38	9.30	0.002	0.36	0.43
$M305_{\downarrow 0.4 \downarrow 0.4}$	0.65	2.47	0.2	0.35	0.26
$M305_{\uparrow 0.4 \uparrow 0.4}$	8.14	0.00	16.57	0.35	0.26
$M305_{\uparrow 0.67 \uparrow 0.67}$	57.16	0.00	25.93	0.35	0.23
$M305q205_{00}$	10.68	24.23	11.22	0.40	0.31
$M305q205_{\uparrow 0.6 0}$	17.31	0.32	27.09	0.36	0.22
$M410_{00}$	0.02	0.00	0.001	0.38	0.27
$M410_{\downarrow 0.65 \uparrow 0.65}$	17.47	4.10	6.25	0.37	0.35
$M410_{\downarrow 0.65 \downarrow 0.65}$	0.00	0.00	0.00	0.00	0.00
$M410_{\uparrow 0.67 \uparrow 0.67}$	46.94	0.04	23.16	0.47	0.28

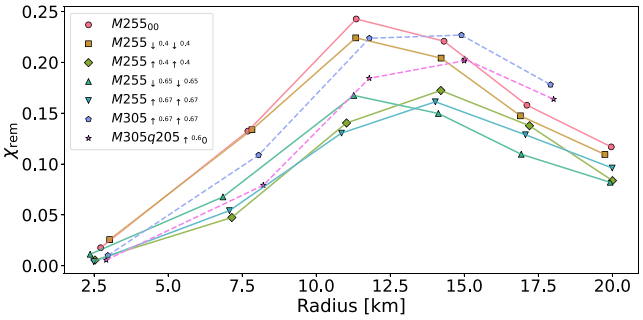

Figure 7. The quasi-local dimensionless spin of the post-merger remnant as a function of radius for models that result in a long-lived NS. Dashed lines represent models with $M_{\rm tot} = 3.05$ M$_\odot$, showing the impact of total mass and mass asymmetry on the spin profile.

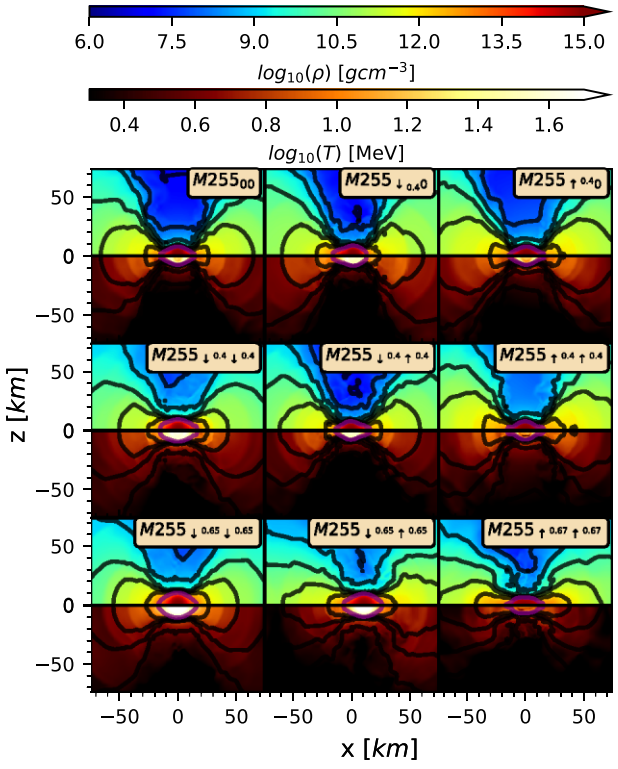

Figure 8. Temperature and rest-mass density distribution in the x–z plane, showing the disc structure at 20 ms after the merger for models with $M_{\rm tot} = 2.55$ M$_\odot$. The rest-mass density contours are the same as in Fig. 3.

yield compact, high-density remnants. Prior to merger, NSs in anti-aligned spins undergo significant elongation, likely influenced by a combination of tidal, spin–orbit and spin–spin interactions. In contrast, aligned spin models have increased equatorial bulge and are therefore more prone to tidal disruption. This is particularly evident in the $M255_{\downarrow 0.65 \uparrow 0.65}$ model, which exhibits the most pronounced tidal tail. The results demonstrate that spin magnitude and orientation play a key role in determining the likelihood of tidal disruption, hence the post-merger remnant.

Disc mass: The rest-mass density and temperature of the disc in the x–z plane, shown in Fig. 8, illustrate the impact of spin on these properties. Aligned spin models exhibit a more neutron-rich disc compared to both irrotational and anti-aligned spin models. This enhanced neutron abundance is generally associated with higher opacities and dimmer kilonovae (D. Kasen, N. R. Badnell & J. Barnes 2013). However, since we do not perform radiative transfer or light-curve analysis in this study, we refrain from drawing quantitative conclusions about the EM counterpart. These aspects will be explored in future work. The disc masses are summarized in Table 3, with their dependence on the effective spin shown in Fig. 9. The figure suggests a correlation between effective spin and disc mass, with linear regression fits derived using the least-squares method. While deviations

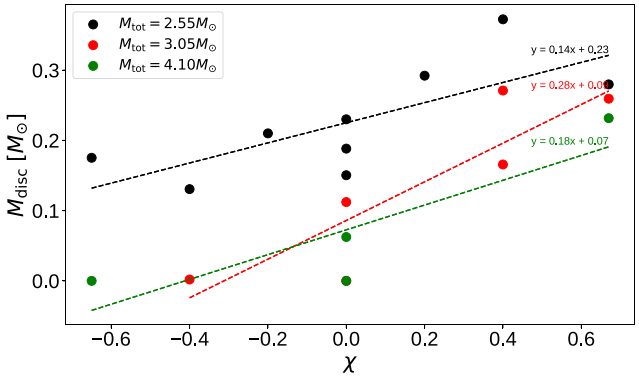

Figure 9. The relationship between effective spin and disc mass. Circles represent different total mass models: $M_{tot} = 2.55$ M$_\odot$ (black), $M_{tot} = 3.05$ M$_\odot$ (red), and $M_{tot} = 4.10$ M$_\odot$ (green). The dashed lines indicate linear regression fits, showing the dependence of disc mass on effective spin and total mass. Even though we have six simulations for $M_{tot} = 3.55$ M$_\odot$, one data point appears to be missing due to the overlap at $\chi = 0$ between two models ($M305_{00}$ and $M410_{00}$). These fits are included solely to illustrate general trends.

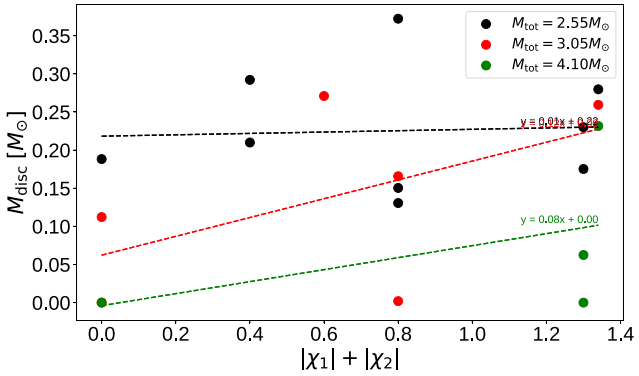

Figure 10. Similar to Fig. 9, but showing the relationship between the sum of individual spin magnitudes and disc mass. The dashed lines represent linear regression fits, included to visualize possible trends. As in Fig. 9, there is an apparent overlap at $|\chi_1| + |\chi_2| = 0$ between models $M305_{00}$ and $M410_{00}$, both of which yield very low disc masses. These fits are included solely to illustrate general trends.

from the fits are evident, possibly due to the LR, the overall trend highlights the importance of the impact of the effective spin on the disc mass. For $M_{tot} = 2.55$ M$_\odot$, the disc mass increases with aligned spins, reaching the maximum of ∼0.4 M$_\odot$ for $M255_{\uparrow 0.4 \uparrow 0.4}$ model, while decreasing with anti-aligned spins. However, for aligned spins beyond $\chi = 0.4$, the disc mass begins to decrease but remains higher than the irrotational model. Single-spin and mixed spin models yield disc masses consistent with the general aligned and anti-aligned models, with variations comparable to the numerical uncertainty between low and high resolution. The relationship between the sum of individual spin magnitudes, $|\chi_1| + |\chi_2|$, and disc mass is also examined, in Fig. 10, as a potential method to constrain individual spins through EM counterparts. The results demonstrate that this relationship depends mildly on the total mass of the binary. For low-mass BNS mergers, $M_{tot} = 2.55$ M$_\odot$, that result in long-lived NSs, disc masses do not show a clear correlation with the sum of individual spin magnitudes. The observed flatness is not interpreted as a physical plateau, but rather as a weak or absent correlation for these models.

5 RESULTS FOR MODELS WITH $M_{tot} = 3.05$ AND 4.10 M$_\odot$

This section explores how the trends identified for different spins in the $M_{tot} = 2.55$ M$_\odot$ models change when considering higher total masses and a different mass ratio.

Inspiral trend: The general inspiral trend persists for high-mass models with anti-aligned (aligned) models merging earlier (later) than the irrotational model. For $M_{tot} = 3.05$ M$_\odot$, the $M305_{\uparrow 0.4 \uparrow 0.4}$ and $M305_{\uparrow 0.67 \uparrow 0.67}$ models show the same change in trend with spin as for $M_{tot} = 2.55$ M$_\odot$. The models with mass asymmetry merge earlier than the equal-mass irrotational and aligned spin models with the same effective spin, due to lower total angular momentum and being tidally disrupted.

Remnants: The fate of the remnant is affected significantly by the total mass, mass asymmetry, and spin. Among the models, only $M305_{\uparrow 0.67 \uparrow 0.67}$ and $M305q205_{\uparrow 0.6 0}$ result in long-lived NSs similarly to the $M_{tot} = 2.55$ M$_\odot$ models. On the other hand, the $M305_{\uparrow 0.4 \uparrow 0.4}$ model results in a delayed collapse to a BH. All other models, regardless of spin, result in prompt BH formation. We test, albeit at LR, the upper limit of the BH spin from BNS mergers. Our analysis shows that $M410_{\uparrow 0.67 \uparrow 0.67}$ model achieves a dimensionless spin parameter of $\chi = 0.92$, becoming the highest spinning BH produced by BNS mergers to date. This surpasses the previously reported limit of $\chi = 0.888 \pm 0.018$ by W. Kastaun et al. (2013). Furthermore, our finding regarding the decrease in BH spin due to delayed collapse and mass asymmetry aligns with the results of S. Bernuzzi et al. (2016) and T. Dietrich et al. (2017a), respectively.

Thermodynamic properties: For the high-mass models, meaningful comparison with $M_{tot} = 2.55$ M$_\odot$ can only be made for models that form long-lived NSs. The $M305_{\uparrow 0.67 \uparrow 0.67}$ model shows stronger shock heating and compression than $M255_{\uparrow 0.67 \uparrow 0.67}$, reaching higher maximum temperature and density due to the increased total mass. The asymmetric mass model $M305q205_{\uparrow 0.6 0}$ reaches a maximum density and temperature of ∼5.4ρ_{sat} and ∼78 MeV, values that are significantly lower in temperature and only slightly lower in density than the $M255_{\downarrow 0.65 \downarrow 0.65}$ model, despite the higher total mass of the asymmetric mass model. This highlights that anti-aligned spins enhance compression more strongly than aligned spins with mass asymmetry, even at higher total mass. Notably, while the $M255_{\downarrow 0.65 \downarrow 0.65}$ model reaches its maximum density almost immediately after merger, the asymmetric mass model shows a delayed density peak, as material gradually accretes. This could be relevant for future EoS studies.

Neutrinos: Same as in the $M_{tot} = 2.55$ M$_\odot$ models, the mean energy hierarchy is unaffected by total mass or mass asymmetry, consistently showing $\langle E_{\nu_x} \rangle > \langle E_{\bar{\nu}_e} \rangle > \langle E_{\nu_e} \rangle$. In contrast, the luminosity hierarchy varies with total mass and mass ratio, reflecting the thermodynamical evolution. For example, the $M305_{\uparrow 0.67 \uparrow 0.67}$ model shows enhanced heavy-lepton production relative to electron neutrinos, yielding $L_{\bar{\nu}_e} > L_{\nu_x} > L_{\nu_e}$ instead of the $L_{\bar{\nu}_e} > L_{\nu_e} > L_{\nu_x}$ for $M255_{\uparrow 0.67 \uparrow 0.67}$. The asymmetric mass model $M305q205_{\uparrow 0.6 0}$, unlike the single-spin aligned model with $M_{tot} = 2.55$ M$_\odot$, shifts to $L_{\nu_x} > L_{\bar{\nu}_e} > L_{\nu_e}$, resembling the pattern observed in irrotational and anti-aligned models with $M_{tot} = 2.55$ M$_\odot$.

GWs: The trend that the irrotational model radiates the highest energy and angular momentum, as seen for $M_{tot} = 2.55$ M$_\odot$, generally holds for higher mass models. However, for $M_{tot} = 3.05$ M$_\odot$, model $M305_{\uparrow 0.4 \uparrow 0.4}$ with a delayed collapse, the radiation exceeds that of the irrotational model, which is consistent with additional post-merger emission preceeding BH formation (as calculated at ∼10 ms after collapse). Increasing the amount of aligned spin

reduces the energy and angular momentum loss, as seen in the $M_{\rm tot} = 2.55$ M$_\odot$ models. Comparing $M305_{\uparrow 0.4 \uparrow 0.4}$ and asymmetric mass model $M305q205_{\uparrow 0.6 0}$ shows that mass asymmetry strongly suppresses energy and angular momentum losses, even given the same effective spin. For $M_{\rm tot} = 4.10$ M$_\odot$, all models promptly collapse to a BH, with the irrotational model showing the largest emission, same as for $M_{\rm tot} = 2.55$ M$_\odot$.

Ejecta and disc: For both $M_{\rm tot} = 3.05$ and 4.10 M$_\odot$, models with anti-aligned spin promptly collapse to a BH and produce a negligible amount of ejecta or none at all. For $M_{\rm tot} = 3.05$ M$_\odot$, mass asymmetry enhances the total amount of ejecta and disc mass through tidal disruption, even in irrotational models. For $M_{\rm tot} = 2.55$ M$_\odot$ models, an increase of spin from $\chi = 0.4$ to 0.67 results in an increase of the total ejecta amount, but reduces the disc mass, whereas for $M_{\rm tot} = 3.05$ M$_\odot$ the disc mass continues to increase, reaching ∼0.26 M$_\odot$. In aligned spin models, fast-moving ejecta is absent for $M_{\rm tot} = 2.55$ and 3.05 M$_\odot$ and negligible for $M_{\rm tot} = 4.10$ M$_\odot$. Overall, disc mass decreases with increasing total mass. This is likely due to prompt collapse reducing the available material. More importantly, even in models that undergo prompt collapse to a BH, mass asymmetry and aligned spins contribute to increased amount of ejecta and disc mass, consistent with T. Dietrich et al. (2017a), who considered irrotational models.

For $\chi = 0.67$, the amount of total ejecta increases slightly comparing $M_{\rm tot} = 2.55$ to 3.05 M$_\odot$, but decreases again for $M_{\rm tot} = 4.10$ M$_\odot$ models, where $M410_{\uparrow 0.67 \uparrow 0.67}$ still yields the largest ejecta and disc mass for the models with the same total mass. This shows that while a high total mass generally suppresses ejecta due to prompt collapse, such high and aligned spin models can still produce a massive amount of ejecta. We note that there is an apparent overlap between models $M305_{00}$ and $M410_{00}$ in Figs 9 and 10, as both models yield very low disc masses (of the order of 10^{-5} M$_\odot$). See Table 3 for the exact values.

We consider the impact of different total masses and mass asymmetry on the relationship between the sum of individual spin magnitudes, $|\chi_1| + |\chi_2|$, and disc mass, as shown in Fig. 10. For low-mass models ($M_{\rm tot} = 2.55$ M$_\odot$), the disc mass remains nearly constant across different spin magnitudes. In contrast, for higher mass models ($M_{\rm tot} = 3.05$ and 4.10 M$_\odot$), the disc mass exhibits a slight increasing trend with spin magnitude. These findings suggest that EM counterparts could offer valuable insights into the individual spins of NSs by measuring disc mass, particularly models undergoing prompt collapse to a BH in equal-mass, irrotational configurations.

6 DISCUSSION AND CONCLUSION

We study the effect of the spin in BNS mergers. We consider 19 configurations with 3 different total masses and having both equal and unequal mass. Also spin configurations are varied, to cover cases where both stars' spins are aligned, or anti-aligned or mixed, with respect to the orbital spin. We investigate the impact of the initial spin on gravitational radiation emission, on properties of ejected matter, and on thermodynamic properties of all these systems as well as GW strains, their detectability, the maximum temperature, the rest-mass density of matter, the neutrino energies, luminosities, and disc masses.

Spin fundamentally alters the orbital dynamics, NS structure, GW emission, ejecta, and disc masses. Its magnitude and orientation influences the duration of the inspiral phase through spin–orbit, spin–spin, and tidal interactions. We find that spin–orbit interactions dominate until $|\chi| = 0.4$, with aligned (anti-aligned) spins extending (shortening) the inspiral phase due to their attractive (repulsive) behaviour, a trend consistent with previous studies (W. Kastaun et al. 2013; P. Tsatsin & P. Marronetti 2013; S. Bernuzzi et al. 2014; T. Dietrich et al. 2017b; W. E. East et al. 2019). Beyond this threshold, spin–spin interactions become significant and counteract the effects of spin–orbit interactions, leading to earlier (later) mergers for aligned (anti-aligned) spins. Although this change in trend is observed in both low and high resolutions, its significance may diminish at higher resolutions.

Thermodynamic properties, such as maximum rest-mass density and temperature, are unaffected by this change in trend. Aligned (anti-aligned) spins consistently result in less (more) violent mergers, reaching lower (higher) maximum rest-mass densities and temperatures compared to the irrotational model. These values peak at ∼145 MeV and $5.6\rho_{\rm sat}$ for the highly anti-aligned spin model. Neither the spin magnitude nor its orientation alters the energy hierarchy among neutrino flavours: heavy-lepton neutrinos are the most energetic, while electron neutrinos are the least energetic. Total neutrino energies and luminosities do not show a monotonic trend with spin orientation. Aligned (anti-aligned) spins tend to suppress (enhance) the overall neutrino number flux, resulting in lower (higher) neutrino energies and luminosities. This behaviour also alters the luminosity hierarchy among flavours, with aligned spins favouring dominant $\bar{\nu}_{\rm e}$ emission, while anti-aligned spins preserve the typical hierarchy with ν_x remaining dominant.

Spin significantly influences the structure of the remnant NS, with aligned spin producing extended spiral arms as a result of redistribution of additional angular momentum. Anti-aligned spins, on the other hand, lead to a significant elongation of the stars prior to merger, consistent with R. Dudi et al. (2022), who studied the maximum anti-aligned spin of $\chi = -0.28$. For aligned spins, the additional angular momentum increases the rotational support of the remnant, in agreement with W. E. East et al. (2019) and S. V. Chaurasia et al. (2020), while anti-aligned spins reduce rotational support, consistent with R. Dudi et al. (2022).

Spin asymmetries, such as models where only one component has spin or models with mixed aligned and anti-aligned spins, exhibit behaviour similar to mass asymmetry. This finding aligns with S. Rosswog et al. (2023, 2024). Additionally, we observe that spin mimics the behaviour of different EoS; this agrees with W. E. East et al. (2019), where degeneracies between spin and EoS were reported. Similarly, T. Dietrich et al. (2017b) identified degeneracies between spin effect, mass ratios, and EoSs, reporting that the influence of spin was smaller than the mass ratios considering spins of $\chi = 0.1$.

Mergers with aligned spins radiate more energy and angular momentum through GWs than anti-aligned spins, yet the irrotational model exhibits the highest overall energy and angular momentum release. We observe changes in both the one-arm and fundamental mode frequencies with spin. For models with $M_{\rm tot} = 2.55$ M$_\odot$, fundamental mode frequencies shift to higher values for aligned spins compared to the irrotational model, consistent with T. Dietrich et al. (2017b), but contrasting with S. Bernuzzi et al. (2014), W. E. East et al. (2019), and S. Rosswog et al. (2024). The impact of increasing aligned spin on the frequency shift is minimal, around ∼10 Hz for $M_{\rm tot} = 2.55$ M$_\odot$, but increases to ∼400 Hz for higher total mass models, highlighting the dependence of the shift on total mass. Conversely, fundamental mode frequencies shift to lower values for anti-aligned spins compared to the irrotational model. This behaviour differs from the findings by W. E. East et al. (2019), who reported that aligned spins shift to lower frequencies and anti-aligned spins shift to higher frequencies for maximum spins of −0.13 (anti-aligned) and 0.33 (aligned), as compared to the irrotational model. For the

one-arm mode, our HR simulations show that its frequency increases by at most ∼30 Hz for aligned spins, while it increases significantly up to ∼1120 Hz for the highly anti-aligned spin model.

Examining the rotation profile of the remnant NSs, we observe that the core rotates more slowly than the envelope, consistent with the findings of M. Shibata & K. Taniguchi (2006), W. Kastaun & F. Galeazzi (2015), and W. E. East et al. (2019). The maximum spin is reached for the irrotational model, also in agreement with W. Kastaun & F. Galeazzi (2015). Additionally, we test the formation of the fastest spinning BH from BNS mergers and find that our $M410_{\uparrow 0.67 \uparrow 0.67}$ model produces the fastest spinning BH to date, with a dimensionless spin of $\chi = 0.92$, surpassing the previously reported limit of $\chi = 0.888 \pm 0.018$ by W. Kastaun et al. (2013). However, it is important to emphasize that this result requires further confirmation with higher resolution.

Beyond its influence on remnant structure, spin significantly affects the total mass and composition of the ejecta, including its fast-moving component. The ejecta mass is strongly dependent on both the magnitude and orientation of the spin. All spin configurations studied result in higher total ejected mass compared to the irrotational model. The composition generally is more neutron rich for aligned spins than anti-aligned spins. Notably, we observe that if only one component has spin, the behaviour differs from models where both components are spinning. Specifically, in models with one spinning component, anti-aligned spin produces more ejecta than aligned spin, whereas in models where both components are spinning, aligned spins result in more ejected mass than anti-aligned models. In the literature, W. Kastaun & F. Galeazzi (2015) reported that spinning models result in lower ejecta mass compared to the irrotational model, which contrasts with our findings, where the irrotational model yields the least total ejecta mass. W. E. East et al. (2019) found that anti-aligned spins result in more ejecta than aligned spins for spin in the range $\chi = -0.13$ to 0.33, and similar results were reported by S. V. Chaurasia et al. (2020) for $\chi = 0.096$. These studies are inconsistent with our findings. However, we do observe the presence of fast-moving ejecta in anti-aligned spins, which aligns with W. E. East et al. (2019). Furthermore, R. Dudi et al. (2022), who explored spins in the interval $\chi = -0.28$ to 0.58, reported that aligned spins result in higher ejecta mass than anti-aligned spins, consistent with our results.

Spin also influences the disc mass. For $M_{\rm tot} = 2.55\ {\rm M}_{\odot}$, aligned spins lead to higher disc masses, while anti-aligned spins result in lower disc masses compared to the irrotational model. The increase in disc mass with aligned spins aligns with findings by W. E. East et al. (2019), S. V. Chaurasia et al. (2020), S. Rosswog et al. (2024), and F. Schianchi et al. (2024). Notably, the disc mass peaks at $\chi = 0.4$ for aligned spins and decreases beyond this value, whereas it continues to increase for anti-aligned spins. In contrast, for $M_{\rm tot} = 3.05\ {\rm M}_{\odot}$, the disc mass continues to increase even for aligned spins exceeding $\chi = 0.4$, highlighting the influence of total mass on this relationship. This suggests that the effective spin could also be constrained using EM counterparts, providing an additional avenue to complement GW observations.

In addition to the dependence of disc mass on effective spin, as shown in Fig. 9, where disc mass increases (decreases) with positive (negative) effective spin, we analyse its variation with the sum of individual spin magnitudes, $|\chi_1| + |\chi_2|$, in Fig. 10 as a potential method to constrain individual spins. We find that this relationship depends on the total mass of the binary. For $M_{\rm tot} = 2.55\ {\rm M}_{\odot}$, the disc mass remains relatively constant across different spins, while higher total mass models exhibit an increase in disc mass with spin. These findings emphasize the importance of considering high spin configurations when investigating EM counterparts, even for equal-mass binaries that undergo prompt collapse to a BH. Since disc mass is the quantity with the most impact on the kilonovae peak luminosity, this finding suggests that one could use EM data to constrain $|\chi_1| + |\chi_2|$, breaking the degeneracy in the measurement of spin from GW alone for models with total mass that leads to prompt BH formation for equal-mass, irrotational model.[1]

Although the spin values and mass ratio investigated in this study are higher than what has been observed, we demonstrate the significant impact of such high spins on GW emissions and properties of ejected matter. These findings suggest that systems with high spins can be identified through GW observations. However, the differences in potential EM counterparts are not explored in this study.

ACKNOWLEDGEMENTS

We would like to thank the anonymous referee for their time provided generously, their invaluable comments, and multiple very detailed suggestions all of which significantly improved both the content and the readability of this paper. RM and BK would like to thank Ian Hawke for his comments and suggestions, guidance, and support. BK would like to thank Roland Haas for his constant support, guidance, and his useful comments and suggestions on every part of the study, David Radice for his many useful comments and suggestions, help, and guidance, Wolfgang Tichy for his support and guidance, and Zachariah B. Etienne for his valuable comments.

Part of the study was presented at Thematic school GWsNS-2023: Gravitational Waves from Neutron Stars and at the European Einstein Toolkit Meeting 2023.

This work used TACC Stampede at XSEDE through allocation PHY160053 from the Extreme Science and Engineering Discovery Environment (XSEDE), which was supported by National Science Foundation grant number #1548562. The work has been performed under the Project HPC-EUROPA3 (INFRAIA-2016-1-730897), with the support of the EC Research Innovation Action under the H2020 Programme; in particular, BK gratefully acknowledges the support of The University of Edinburgh and the computer resources and technical support provided by EPCC. The numerical calculations reported in this paper were partially performed at TUBITAK ULAKBIM, High Performance and Grid Computing Center (TRUBA resources).

DATA AVAILABILITY

The data generated in this article are available for a reasonable request from the corresponding author.

REFERENCES

Abbott B. P. et al., 2017a, Phys. Rev. Lett., 119, 161101
Abbott B. P. et al., 2017b, ApJ, 848, L12
Abbott B. P. et al., 2017c, ApJ, 848, L13
Abbott B. P. et al., 2019a, Phys. Rev. X, 9, 011001
Abbott B. P. et al., 2019b, Phys. Rev. Lett., 123, 011102
Abbott B. P. et al., 2020, ApJ, 892, L3
Acernese F. et al., 2015, Class. Quantum Gravity, 32, 024001
Allen G., Goodale T., Masso J., Seidel E., 1999, Proceedings. The Eighth International Symposium on High Performance Distributed Computing (Cat. No.99TH8469), The Cactus Computational Toolkit and Using Distributed Computing to Collide Neutron Stars. IEEE, Piscataway, USA, p. 57

[1] Radice (private communication).

Baker T., Bellini E., Ferreira P. G., Lagos M., Noller J., Sawicki I., 2017, Phys. Rev. Lett., 119, 251301
Banyuls F., Font J. A., Ibáñez J. M., Martí J. M., Miralles J. A., 1997, ApJ, 476, 221
Baumgarte T. W., Shapiro S. L., 1998, Phys. Rev. D, 59, 024007
Bauswein A., Janka H. T., 2012, Phys. Rev. Lett., 108, 011101
Bauswein A., Baumgarte T. W., Janka H. T., 2013, Phys. Rev. Lett., 111, 131101
Bauswein A., Stergioulas N., Janka H.-T., 2016, Eur. Phys. J. A, 52, 56
Bernuzzi S., Hilditch D., 2010, Phys. Rev. D, 81, 084003
Bernuzzi S., Dietrich T., Tichy W., Brügmann B., 2014, Phys. Rev. D, 89, 104021
Bernuzzi S., Radice D., Ott C. D., Roberts L. F., Moesta P., Galeazzi F., 2016, Phys. Rev. D, 94, 024023
Brown J. D., Diener P., Sarbach O., Schnetter E., Tiglio M., 2009, Phys. Rev. D, 79, 044023
Cactus developers, 2023a, Cactus Computational Toolkit. Available at: https://www.cactuscode.org (accessed 2025 October 2)
Cactus developers, 2023b, Cactus Computational Toolkit Prizes. Available at: https://www.cactuscode.org/media/prizes (accessed 2025 October 2)
Camilletti A., Perego A., Guercilena F. M., Bernuzzi S., Radice D., 2024, Phys. Rev. D, 109, 063023
Campanelli M., Lousto C. O., Zlochower Y., 2006, Phys. Rev. D, 74, 041501
Chaurasia S. V., Dietrich T., Ujevic M., Hendriks K., Dudi R., Fabbri F. M., Tichy W., Brügmann B., 2020, Phys. Rev. D, 102, 024087
Cutler C., Flanagan E., 1994, Phys. Rev. D, 49, 2658
Cutler C. et al., 1993, Phys. Rev. Lett., 70, 2984
Deppe N. et al., 2024, Class. Quantum Gravity, 41, 245002
Dietrich T., Bernuzzi S., Ujevic M., Brügmann B., 2015a, Phys. Rev. D, 91, 124041
Dietrich T., Moldenhauer N., Johnson-McDaniel N. K., Bernuzzi S., Markakis C. M., Bruegmann B., Tichy W., 2015b, Phys. Rev. D, 92, 124007
Dietrich T., Ujevic M., Tichy W., Bernuzzi S., Brügmann B., 2017a, Phys. Rev. D, 95, 024029
Dietrich T., Bernuzzi S., Ujevic M., Tichy W., 2017b, Phys. Rev. D, 95, 044045
Dietrich T., Bernuzzi S., Brügmann B., Ujevic M., Tichy W., 2018, Phys. Rev. D, 97, 064002
Dietrich T., Coughlin M. W., Pang P. T. H., Bulla M., Heinzel J., Issa L., Tews I., Antier S., 2020, Science, 370, 1450
Dreyer O., Krishnan B., Shoemaker D., Schnetter E., 2003, Phys. Rev. D, 67, 024018
Dudi R., Dietrich T., Rashti A., Brügmann B., Steinhoff J., Tichy W., 2022, Phys. Rev. D, 105, 064050
East W. E., Paschalidis V., Pretorius F., Shapiro S. L., 2016, Phys. Rev. D, 93, 024011
East W. E., Paschalidis V., Pretorius F., Tsokaros A., 2019, Phys. Rev. D, 100, 124042
Eichler D., Livio M., Piran T., Schramm D. N., 1989, Nature, 340, 126
Einfeldt B., 1988, SIAM J. Numer. Anal., 25, 294
Espino P. L., Radice D., Zappa F., Gamba R., Bernuzzi S., 2024, Phys. Rev. D, 109, 103027
Etienne Z. B., Liu Y. T., Shapiro S. L., Baumgarte T. W., 2009, Phys. Rev. D, 79, 044024
Fields J., Zhu H., Radice D., Stone J. M., Cook W., Bernuzzi S., Daszuta B., 2025, ApJS, 276, 35
Finn L. S., Chernoff D. F., 1993, Phys. Rev. D, 47, 2198
Flanagan E. E., Hinderer T., 2008, Phys. Rev. D, 77, 021502
Foucart F., 2023, Living Rev. Comput. Astrophys., 9, 1
Foucart F., O'Connor E., Roberts L., Kidder L. E., Pfeiffer H. P., Scheel M. A., 2016, Phys. Rev. D, 94, 123016
Foucart F., Duez M. D., Hébert F., Kidder L. E., Kovarik P., Pfeiffer H. P., Scheel M. A., 2021, ApJ, 920, 82
Foucart F., Chi-Kit Cheong P., Duez M. D., Kidder L. E., Pfeiffer H. P., Scheel M. A., 2024, Phys. Rev. D, 110, 083028
Gittins F., Matur R., Andersson N., Hawke I., 2025, Phys. Rev. D, 111, 023049
Goldstein A. et al., 2017, ApJ, 848, L14
Goodale T., Allen G., Lanfermann G., Massó J., Radke T., Seidel E., Shalf J., 2003, in Palma J. M. L. M., Sousa A. A., Dongarra J., Hernández V., eds, Lecture Notes in Computer Science, Vol. 2565, High Performance Computing for Computational Science – VECPAR 2002. Springer, Berlin, Heidelberg, p. 197
Gottlieb S., Ketcheson D. I., Shu C.-W., 2009, J. Sci. Comput., 38, 251
Grandclement P., 2010, J. Comput. Phys., 229, 3334
Haas R. et al., 2022, The Einstein Toolkit, Zenodo. Available at: https://doi.org/10.5281/zenodo.7245853
Hallinan G. et al., 2017, Science, 358, 1579
Hild S. et al., 2011, Class. Quantum Gravity, 28, 094013
Hilditch D., Bernuzzi S., Thierfelder M., Cao Z., Tichy W., Brügmann B., 2013, Phys. Rev. D, 88, 084057
Hinderer T., 2008, ApJ, 677, 1216
Hinderer T., Lackey B. D., Lang R. N., Read J. S., 2010, Phys. Rev. D, 81, 123016
Hotokezaka K., Kiuchi K., Shibata M., Nakar E., Piran T., 2018, ApJ, 867, 95
Kafka P., 1988, in Burke W. R., ed., ESA SP-283, Space Science and Fundamental Physics. ESA, Noordwijk, p. 121
Kasen D., Badnell N. R., Barnes J., 2013, ApJ, 774, 25
Kasen D., Metzger B., Barnes J., Quataert E., Ramirez-Ruiz E., 2017, Nature, 551, 80
Kasliwal M. M. et al., 2017, Science, 358, 1559
Kastaun W., 2021, Astrophysics Source Code Library, record ascl:2107.017
Kastaun W., Galeazzi F., 2015, Phys. Rev. D, 91, 064027
Kastaun W., Galeazzi F., Alic D., Rezzolla L., Font J. A., 2013, Phys. Rev. D, 88, 021501
Kastaun W., Ciolfi R., Giacomazzo B., 2016, Phys. Rev. D, 94, 044060
Lattimer J. M., 2012, Annu. Rev. Nucl. Part. Sci., 62, 485
LIGO Collaboration, 2022, Advanced LIGO Sensitivity for the O4 Run. Available at: https://dcc.ligo.org/public/0180/T2200043/003/aligo_O4high.txt (accessed October 2, 2025)
Löffler F. et al., 2012, Class. Quantum Gravity, 29, 115001
Maggiore M. et al., 2020, J. Cosmol. Astropart. Phys., 2020, 050
Margalit B., Metzger B. D., 2017, ApJ, 850, L19
Marronetti P., Shapiro S. L., 2003, Phys. Rev. D, 68, 104024
Nakamura T., Oohara K., Kojima Y., 1987, Prog. Theor. Phys. Suppl., 90, 1
O'Connor E., Ott C. D., 2010, Class. Quantum Gravity, 27, 114103
Papenfort L. J., Tootle S. D., Grandclément P., Most E. R., Rezzolla L., 2021, Phys. Rev. D, 104, 024057
Papenfort L. J., Most E. R., Tootle S., Rezzolla L., 2022, MNRAS, 513, 3646
Paschalidis V., East W. E., Pretorius F., Shapiro S. L., 2015, Phys. Rev. D, 92, 121502
Pian E. et al., 2017, Nature, 551, 67
Piran T., 1992, ApJ, 389, L45
Pollney D., Reisswig C., Schnetter E., Dorband N., Diener P., 2011, Phys. Rev. D, 83, 044045
Poudel A., Tichy W., Brügmann B., Dietrich T., 2020, Phys. Rev. D, 102, 104014
Radice D., 2017, ApJ, 838, L2
Radice D., 2020, Symmetry, 12, 1249
Radice D., 2023, Scientific Data Library. Available at: https://bitbucket.org/dradice/scidata (accessed 2025 October 2)
Radice D., Bernuzzi S., 2023, ApJ, 959, 46
Radice D., Hawke I., 2024, Living Rev. Comput. Astrophys., 10, 1
Radice D., Rezzolla L., 2012, A&A, 547, A26
Radice D., Rezzolla L., Galeazzi F., 2014a, Class. Quantum Gravity, 31, 075012
Radice D., Rezzolla L., Galeazzi F., 2014b, MNRAS, 437, L46
Radice D., Rezzolla L., Galeazzi F., 2015, in Pogorelov N. V., Audit E., Zank G. P., eds, ASP Conf. Ser. Vol. 498, Numerical Modeling of Space Plasma Flows ASTRONUM-2014. Astron. Soc. Pac., San Francisco, p. 121
Radice D., Bernuzzi S., Ott C. D., 2016a, Phys. Rev. D, 94, 064011
Radice D., Galeazzi F., Lippuner J., Roberts L. F., Ott C. D., Rezzolla L., 2016b, MNRAS, 460, 3255
Radice D., Perego A., Zappa F., Bernuzzi S., 2018a, ApJ, 852, L29

Radice D., Perego A., Hotokezaka K., Fromm S. A., Bernuzzi S., Roberts L. F., 2018b, ApJ, 869, 130
Radice D., Perego A., Hotokezaka K., Bernuzzi S., Fromm S. A., Roberts L. F., 2018c, ApJ, 869, L35
Radice D., Bernuzzi S., Perego A., Haas R., 2022, MNRAS, 512, 1499
Rashti A., Noe A., 2025, Class. Quantum Gravity, 42, 015007
Read J. S. et al., 2013, Phys. Rev. D, 88, 044042
Reisswig C., Pollney D., 2011, Class. Quantum Gravity, 28, 195015
Rosswog S., Torsello F., Diener P., 2023, Front. Appl. Math. Stat., 9 1236586
Rosswog S., Diener P., Torsello F., Tauris T. M., Sarin N., 2024, MNRAS, 530, 2336
Ruffert M., Janka H. T., 2001, A&A, 380, 544
Ruffert M., Janka H. T., Schäfer G., 1995, Ap&SS, 231, 423
Ruffert M., Janka H. T., Takahashi K., Schaefer G., 1997, A&A, 319, 122
Sakstein J., Jain B., 2017, Phys. Rev. Lett., 119, 251303
Schianchi F., Ujevic M., Neuweiler A., Gieg H., Markin I., Dietrich T., 2024, Phys. Rev. D, 109, 123011
Schnetter E., Hawley S. H., Hawke I., 2004, Class. Quantum Gravity, 21, 1465
Sekiguchi Y., Kiuchi K., Kyutoku K., Shibata M., 2015, Phys. Rev. D, 91, 064059
Shibata M., Nakamura T., 1995, Phys. Rev. D, 52, 5428
Shibata M., Taniguchi K., 2006, Phys. Rev. D, 73, 064027
Smartt S. J. et al., 2017, Nature, 551, 75
Steiner A. W., Hempel M., Fischer T., 2013, ApJ, 774, 17
Stellarcollapse, 2017, stellarcollapse.org. Available at: https://stellarcollapse.org (accessed 2025 October 2)
Suresh A., Huynh H. T., 1997, J. Comput. Phys., 136, 83
Tacik N. et al., 2015, Phys. Rev. D, 92, 124012
The Einstein Toolkit, 2025, The Einstein Toolkit. Available at: https://einsteintoolkit.org (accessed 2025 October 2)
The LIGO Scientific Collaboration, 2015, Class. Quantum Gravity, 32, 074001
The LIGO Scientific Collaboration, The Virgo Collaboration, 2018, Phys. Rev. Lett., 121, 161101
Thornburg J., 1996, Phys. Rev. D, 54, 4899
Thornburg J., 2004, Class. Quantum Gravity, 21, 743
Tichy W., 2006, Phys. Rev. D, 74, 084005
Tichy W., 2009a, Class. Quantum Gravity, 26, 175018
Tichy W., 2009b, Phys. Rev. D, 80, 104034
Tichy W., 2011, Phys. Rev. D, 84, 024041
Tichy W., 2012, Phys. Rev. D, 86, 064024
Tichy W., Rashti A., Dietrich T., Dudi R., Brügmann B., 2019, Phys. Rev. D, 100, 124046
Tichy W., Ji L., Adhikari A., Rashti A., Pirog M., 2023, Class. Quantum Gravity, 40, 025004
Troja E. et al., 2017, Nature, 551, 71
Tsatsin P., Marronetti P., 2013, Phys. Rev. D, 88, 064060
Weyhausen A., Bernuzzi S., Hilditch D., 2012, Phys. Rev. D, 85, 024038
Wilson J. R., Mathews G. J., 1995, Phys. Rev. Lett., 75, 4161
Zilhão M., Löffler F., 2013, Int. J. Mod. Phys. A, 28, 1340014

This paper has been typeset from a TEX/LATEX file prepared by the author.